Active Disturbance Rejection Speed Control of IPMSM Drive System Based on Generalized Multifrequency Quasi-Resonant Filter Decoupling Linear Extended State Observer

Yangyang Cui, Zhonggang Yin, *Member, IEEE*, Yanping Zhang, *Member, IEEE*, and Hui Yang

***Abstract*—The dual observation of periodic and aperiodic interferences cannot be balanced by traditional linear extended state observer (T-LESO). Therefore, the speed fluctuations caused by uncertain periodic and aperiodic interferences in the interior permanent magnet synchronous motor control system cannot be suppressed by the traditional linear active disturbance rejection controller. To resolve the aforementioned problem, an improved linear active disturbance rejection controller (I-LADRC) in which multifrequency quasi-resonant filtering decoupling linear extended state observer and generalized linear extended state observer (G-LESO) are cascaded is proposed. In this controller, the interference feedforward control method of T-LESO is first changed, the observer bandwidth ω_o and controller bandwidth ω_c in the transfer function based on the interference term are decoupled from each other, reducing the difficulty of parameter tuning. On this basis, a multifrequency quasi-resonant filter is embedded in the decoupled linear extended state observer (LESO), so that periodic interferences can be accurately observed. For G-LESO, a fourth-order LESO is adopted to enable more accurate observation of aperiodic high-order interferences. The outer loop controller based on I-LADRC is designed, and the correctness and effectiveness of this method are verified through experiments.**

***Index Terms*—Active disturbance rejection controller, extended state observer, generalized, multifrequency quasi-resonant filter decoupling, periodic and aperiodic interferences.**

I. Introduction

As a core component of advanced manufacturing, high-performance permanent magnet synchronous motor (PMSM) has been widely used in modern industry due to its high power density and small size [1]. For example, in the field of electric and hybrid vehicles, PMSM is used as the main power source to drive the wheels, and its range can be extended by its high efficiency and lightweight characteristics [2]. In the field of computer numerical control (CNC) machine tools and industrial robots, PMSM is mainly used for spindle drive in CNC machine tools and joint drive in industrial robots. In the field of variable frequency air conditioning and refrigerators, energy-saving and silent operation can be achieved through PMSM variable frequency speed regulation [3]. Meanwhile, high-power PMSM is widely used as a traction motor in subways and high-speed railways. In addition, PMSM has gradually been applied to fields such as national defense and military. In the abovementioned applications, speed control is the core requirement of the PMSM drive system, specifically manifested as follows [4], [5]: (1) in terms of dynamic response capability, industrial robots, and CNC machine tools are required to respond quickly to instructions (in milliseconds) to avoid machining errors. The acceleration/deceleration of electric vehicles needs to be smoothly transitioned. (2) In terms of high precision and stability, in precision manufacturing scenarios, motors need to maintain stable torque at low speeds (even close to zero speed) to avoid crawling phenomena. In addition, its vibration and noise need to be suppressed at high speeds. (3) In terms of wide speed regulation range, wind power generation needs to adapt to a wide speed range of wind speed changes (such as 1:10). The full range of electric vehicles from low-speed climbing to high-speed cruising needs to be covered. (4) In terms of energy efficiency optimization, minimizing copper and iron losses can be achieved through precise speed control, such as reducing standby power consumption in variable frequency appliances. (5) In terms of anti-interference ability, robust control algorithms are required to maintain a constant speed in response to sudden load changes (such as changes in machine tool cutting force) or power grid fluctuations. In addition, compared to the surface-mounted PMSM field-oriented control system based on zero d-axis control, the reluctance torque caused by the unequal dq-axes inductance can be utilized by the interior permanent magnet synchronous motor (IPMSM) field-oriented control system based on maximum torque per ampere control, and the control system ability to carry load torque is further improved [6], [7]. Therefore, the IPMSM is more widely used than surface-mounted PMSM. The stable operation of the IPMSM control

Received 20 November 2024; revised 24 February 2025; accepted 20 March 2025. Date of publication 25 March 2025; date of current version 26 May 2025. This work was supported in part by the National Natural Science Foundation of China under Grant 52177194 and Grant 52207222, in part by the China Postdoctoral Science Foundation under Grant 2022M722559, and in part by the Science and Technology Innovation Team in Shaanxi Province under Grant 2023-CX-TD-23. Recommended for publication by Associate Editor A. M. Trzynadlowski. *(Corresponding author: Zhonggang Yin.)*

The authors are with the Department of Electrical Engineering, Xi'an University of Technology, Xi'an 710054, China (e-mail: 1211913014@stu.xaut.edu.cn; zhgyin@xaut.edu.cn; zhangyanping@xaut.edu.cn; ivyyang@xaut.edu.cn).

Color versions of one or more figures in this article are available at https://doi.org/10.1109/TPEL.2025.3554701.

Digital Object Identifier 10.1109/TPEL.2025.3554701

system relies on smooth speed regulation, and its performance is mainly influenced by the outer loop controller.

The IPMSM control system is usually affected by multiple sources of interference such as the system itself and external factors during its operation [8]. There are various types of multisource interferences, which can be summarized into two categories based on their variation patterns: periodic and aperiodic interferences. As for the entire IPMSM dual loop vector control system, periodic interferences mainly include system friction, sampling errors, inverter nonlinearity, periodic load interferences, and unmodeled dynamic periodic interferences [9]. Aperiodic interferences mainly include: parameter mismatch, system delay, cross coupling, aperiodic load interferences, and unmodeled dynamic aperiodic interferences [10]. The abovementioned interferences will to some extent cause speed fluctuations and torque pulsations in the motor, which will have various impacts on the control performance of the system. The specific manifestations are as follows [11], [12]: (1) Damage to the mechanical system. The wear of bearings, gears, and shafts will accelerate due to continuous vibration, and the service life of the motor will be shortened. (2) Decreased control performance. Iron and copper losses will increase due to torque pulsation, and the overall efficiency of the system will be reduced. (3) Risk of operational stability. The resonance of the system may be triggered by specific frequency pulsations, leading to catastrophic failures. (4) Electromagnetic compatibility problems. Other devices are interfered with by high-frequency pulsation through the power line, which affects the overall electromagnetic compatibility performance of the system. In addition, under low-speed heavy load conditions, the phenomenon of "crawling" may be caused by torque pulsation, which affects the stability of the system. In order to better suppress the multisource interferences mentioned earlier, the control performance of the system can be further improved, and many interference suppression methods have been applied in the IPMSM control system [13]. Proportional integral (PI) control has always held a dominant position in ac motor speed control systems because of its inherent advantages [14]. However, due to the sensitivity of traditional PI controllers to parameters and poor adaptability to load changes, the speed fluctuations caused by periodic and aperiodic interferences in IPMSM control systems cannot be suppressed by it. Therefore, in order to address the insufficient ability of PI controllers to suppress periodic and aperiodic interferences, other interference suppression methods, such as genetic algorithm based PI control, Kalman filter based feedback control [15], quasi-proportional resonance control, composite control, and active disturbance rejection control (ADRC), have gradually been used to interference suppression in motor control systems. Among them, the ADRC is proposed by Han [16] in which the natural interference resistance of PI controllers in classical control theory with the system model independence and the state observation concept in modern control theory. The core idea is to use the integral series as the standard type, the nonlinear extended state observer and nonlinear state error feedback are used to suppress the lumped interference received by the system. However, the nonlinear ADRC structure is complex and requires numerous parameters to be adjusted. At the same time, it is difficult to determine its stability boundary using frequency domain analysis methods, making it difficult to promote and apply in the field of industrial control. To solve the aforementioned problem, a linear active disturbance rejection controller (LADRC) is designed by Gao [17]. All components of the controller are linearized, and all adjustable parameters are bandwidth adjusted. This not only clarifies the physical meaning of the controller parameters but also enables the use of frequency domain analysis to analyze its control performance. However, the traditional linear active disturbance rejection controller (T-LADRC) has inherent limitations and cannot suppress high-order and periodic interferences. Therefore, it is necessary to propose corresponding improvement plans for LADRC based on the characteristics of different interferences in the IPMSM control system.

At present, in order to suppress multisource interferences in alternating current motor control systems, numerous researchers have proposed different improvement schemes for ADRC, which have been applied in alternating current motor control systems to achieve high-performance control. In [18], a novel LADRC based on complex coefficient linear extended state observer (LESO) is designed and applied to the inner loop controller of PMSM control systems to suppress periodic harmonic interferences in the inner loop. This controller is based on the internal model principle and introduces a complex coefficient filter with frequency selection and phase sequence discrimination characteristics in traditional linear extended state observer (T-LESO), thereby improving the accuracy of periodic harmonic interference observation. In [19], a novel LADRC based on series leading correction LESO is proposed. In this controller, the range of lumped interference observation is expanded without increasing the ω_o condition, and the ability to resist load interference is improved. In [20], an enhanced LADRC with a compensation function observer is designed and applied to the outer loop of the PMSM control system. At the same time, a practical parameter configuration process that combines interference compensation and noise suppression is designed, aiming to resolve the problem of insufficient one-degree-of-freedom characteristics and anti-interference ability in T-LADRC. In [21], an improved LADRC suitable for low-speed operating conditions of PMSM control systems is proposed. By introducing an error proportional feedback term in LESO, the system's ability to observe load interference is enhanced. At the same time, a high-pass filter is used as a speed compensator at the linear state error feedback (LSEF) to suppress the speed ripple caused by periodic interferences during low-speed operation. In [22], LADRC based on proportional derivative feedback control and fourth-order LESO is designed as the outer loop controller of PMSM to improve the low-frequency interference suppression performance. However, when the IPMSM control system is subjected to uncertain periodic and aperiodic interferences (especially high-order interferences), the T-LADRC and many new LADRCs are still unable to reasonably suppress the speed fluctuations caused by the coupling between ω_o and ω_c and their own low-pass filtering characteristics.

To solve the aforementioned problem, an I-LADRC in which multifrequency quasi-resonant filtering decoupling linear

extended state observer (MFQRFD-LESO) and generalized linear extended state observer (G-LESO) are cascaded is proposed. Compared with the methods in the latest existing references, the innovation and contribution of this method are mainly reflected in the following three aspects.

1) For the suppression of periodic interferences, compared with [18], [23], and [24], the interference feedforward control method of T-LESO has been changed, and the decoupling of ω_o and ω_c in the closed-loop transfer function of the system output term based on the interference term has been achieved, resulting in a decoupled LESO. The difficulty of parameter tuning is reduced, and the system's anti-interference ability is improved. Meanwhile, multifrequency quasi-resonant filters are embedded into decoupled LESO, enabling real-time estimation of periodic interferences in the system. Thus, the problem of coupling the new parameters introduced by directly combining the quasi-resonant controller with T-LESO with ω_o and ω_c is solved, which not only reduces the observation accuracy of LESO for periodic interferences but also increases the complexity of parameter tuning.
2) For the suppression of aperiodic interferences, compared with [25] and [26], the impact of aperiodic high-order interferences on the system is mainly solved in this article. Aperiodic interferences are decomposed into a superposition of step interferences (first-order interferences), slope interferences (second-order interferences), and acceleration interferences (third-order interferences). To solve the high-order interferences, a G-LESO based on interference differential compensation is proposed in this article. Therefore, the inability of traditional control methods to make effective estimates of high-order interferences in the system is avoided.
3) The I-LADRC proposed in this article can suppress both periodic and aperiodic high-order interferences in the speed loop of IPMSM drive systems, thereby reducing the speed fluctuations caused by periodic interferences and solving the problem of reduced dynamic response under heavy loads. In this method, the previous idea that a single control method could only suppress a single interference has been abandoned. Its advantage lies in the ability to simultaneously suppress multiple interferences in the system, and the frequency domain analysis method can prove the universality, generality, and selectivity of this method for different interferences.

The rest of this article is organized as follows. In Section II, while the IPMSM motion equation with interference terms is established, a speed loop controller for the IPMSM drive system based on T-LADRC is designed. In Section III, while I-LADRC is proposed, a speed loop controller for the IPMSM drive system based on I-LADRC is designed. In Section IV, the stability, interference rejection, and observational performance of the IPMSM driving system based on I-LADRC are demonstrated and analyzed. In Section V, the parameter tuning principles for the speed loop controller of the IPMSM drive system based on I-LADRC are presented. In Section VI, the correctness and effectiveness of the method are verified through experiments. Section VII provides a summary and outlook.

II. Design of Speed Loop Controller for IPMSM Drive System Based on T-LADRC

The establishment of the IPMSM control system dynamic equation is the basis for designing the outer loop controller, and its motion equation is shown as follows [27]:

$$(\tilde{J} \pm \Delta J)\dot{\omega}_m = T_e^* - T_l - \xi_s \omega_m + (T_e - T_e^*) + \vartheta_s \tag{1}$$

where ω_m is the mechanical angular velocity of IPMSM after rotation transformer and filtering. ξ_s is the viscosity factor. T_e^* and T_e are the given and output torque. T_l is the load torque. ϑ_s is the unmodeled dynamics of the system and other unknown external interferences. ΔJ, $\tilde{J}$, and J are the variation, nominal value, and actual value of the moment of inertia, and $J = \tilde{J} + \Delta J$.

For T_l, the mathematical model that includes possible types of load interferences is shown as follows:

$$T_l = K_s + K_r t + K_a t^2 + \sum_{n=1}^{\infty} (A_{sn} \sin n\omega t + B_{sn} \cos n\omega t) + \gamma_s \tag{2}$$

where K_s, K_r, and K_a are the gains of step interference, ramp interference, and acceleration interference. A_{sn} and B_{sn} are the amplitudes of sinusoidal and cosine load interferences. γ_s is another unknown load interference.

When ω_m and lumped interference f_s are state variables, the state space expression of the IPMSM is as follows [28]:

$$\dot{\omega}_s = f_s + \frac{1}{\tilde{J}} T_e^*. \tag{3}$$

For f_s, its expression is as follows:

$$f_s = \mp \frac{\Delta J}{\tilde{J}} \dot{\omega}_m + \frac{1}{\tilde{J}}(T_e - T_e^*) - \frac{\xi_s}{\tilde{J}} \omega_m - \frac{1}{\tilde{J}} T_l + \frac{1}{\tilde{J}} \vartheta_s. \tag{4}$$

According to (3), the motion equation of IPMSM is a first-order differential equation, so first-order LADRC is used to control it. The main goal of LADRC is to target practical engineering applications. Due to the comprehensive consideration of the current transition process configuration method and the need to avoid high-frequency oscillations, the linear tracking differentiator configuration transition process is omitted in the LADRC simplification scheme. At this time, the first-order T-LADRC is mainly composed of two parts: second-order LESO and LSEF.

For first-order system $\dot{y} = f(x, t, u) + b_0 u$, the system output $y = x_1$ and the lumped interference $f = x_2$ are usually selected as state variables. The expression for first-order T-LADRC is as follows [29], [30]:

$$\begin{cases} \underbrace{\begin{aligned} \dot{z}_1 &= z_2 - \beta_1(z_1 - x_1) + b_0 u_T \\ \dot{z}_2 &= -\beta_2(z_1 - x_1) \end{aligned}}_{\text{T-LESO}} \\ u_T = \frac{k_c(r - z_1) - z_2}{b_0} \end{cases} \tag{5}$$

where z_1 and z_2 are the estimated values of state variables x_1 and x_2, respectively. β_1 and β_2 is the LESO feedback gain

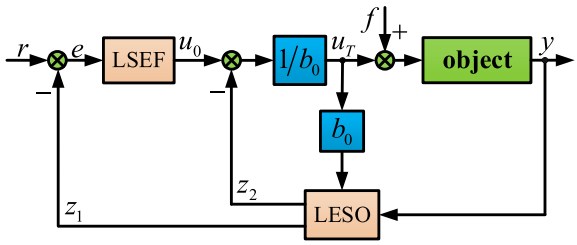

Fig. 1. Structural diagram of first-order T-LADRC.

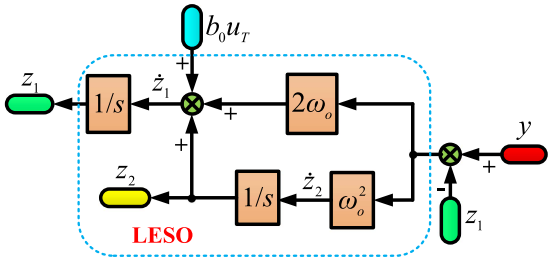

Fig. 2. Structural diagram of second-order T-LESO.

coefficient. b_0 is the compensation factor (it is also known as control gain). k_c is the controller proportional gain coefficient. r is the given input value.

By pole assignment, the β_1 and β_2 are configured at ω_o, the k_c is configured at ω_c.

$$\begin{cases} s^2+\beta_1 s+\beta_2=(s+\omega_o)^2 \\ s+k_c=s+\omega_c \end{cases}. \tag{6}$$

According to (6), $\beta_1=2\omega_o$, $\beta_2=\omega_o^2$, $k_c=\omega_c$.

According to (5) and (6), the structural diagrams of first-order T-LADRC and second-order T-LESO are shown in Figs. 1 and 2, respectively.

According to (3)–(6), the expression for the outer loop controller of the IPMSM control system based on T-LADRC can be obtained as follows:

$$\begin{cases} \dot{\hat{\omega}}_m=\hat{f}_s-2\omega_o(\hat{\omega}_m-\omega_m)+\frac{1}{\bar{J}}T_e^* \\ \dot{\hat{f}}_s=-\omega_o^2(\hat{\omega}_m-\omega_m) \\ T_e^*=\frac{\omega_c(\omega_m^*-\hat{\omega}_m)-\hat{f}_s}{1/\bar{J}} \end{cases} \tag{7}$$

where " ˆ " is the observed value of the state variable. ω_m^* is the given value of ω_m.

Regarding the limitations of first-order T-LADRC, from [31], the second-order T-LESO can be considered a low-pass filter. Therefore, error-free observation of aperiodic or low-order interferences can be only implemented. In addition, for the lumped interference of the same frequency, the observation error of the lumped interference can be reduced by increasing the ω_o of T-LESO. The T-LESO is affected by ω_o and its own low-pass filtering characteristics, making it impossible for T-LADRC to effectively restrain both periodic and aperiodic interferences in the IPMSM control system simultaneously [32]. Therefore, it is necessary to propose corresponding improvement methods for T-LADRC based on different interference characteristics.

III. Design of Speed Loop Controller for IPMSM Drive System Based on I-LADRC

First, the corresponding improvement scheme for T-LADRC is proposed in this section. Then, a speed loop controller for the IPMSM drive system based on I-LADRC is established.

A. Multifrequency Quasi-Resonant Filtering Decoupling Linear Extension State Observer

For T-LADRC, according to (5) and (6), the transfer function $G_{\mathrm{T}}(s)$ based on the interference term is shown as follows:

$$\begin{aligned} G_T(s)&=\frac{Y(s)}{F_s(s)} \\ &=\frac{s^2+(2\omega_o+\omega_c)s}{s^3+(2\omega_o+\omega_c)s^2+(2\omega_o\omega_c+\omega_o^2)s+\omega_o^2\omega_c}. \end{aligned} \tag{8}$$

According to (8), the ω_o and ω_c in $G_{\mathrm{T}}(s)$ of T-LADRC are coupled with each other, thereby increasing the complexity of parameter tuning. To solve this problem, decoupling LADRC (D-LADRC) is proposed as follows:

$$\begin{cases} \dot{z}_1=z_2+b_0u_D \\ \dot{z}_2=-2\omega_{o1}(\dot{z}_1-\dot{x}_1)-\omega_{o1}^2(z_1-x_1) \\ u_D=\frac{\omega_c(r-z_1)-z_2}{b_0} \end{cases} \tag{9}$$

where ω_{o1} is the bandwidth of the decoupled LESO.

By applying the Laplace transform to (9), the $G_{\mathrm{D}}(s)$ of the output term of decoupled LADRC based on the interference term is as follows:

$$G_D(s)=\frac{s}{s^2+2\omega_{o1}s+\omega_{o1}^2}. \tag{10}$$

According to (10), the mutual coupling between ω_{o1} and ω_c is achieved by D-LADRC, and the parameter setting is optimized.

To achieve observation of periodic interferences by LESO, a multifrequency quasi-resonant filter is embedded into (9) to obtain MFQRFD-LESO, which is expressed as follows:

$$\begin{cases} \dot{z}_1=z_2+b_0u_{MFQRFD} \\ \dot{z}_2=-(2\omega_{o1}+q(t))(\dot{z}_1-\dot{x}_1)-\omega_{o1}^2(z_1-x_1) \end{cases} \tag{11}$$

where $q(t)$ refers to multiple $q_1(t)$, $q_2(t)$, $q_3(t)$, $\cdots$ connected in parallel, which can observe periodic interferences of different frequencies.

The time-domain and frequency-domain expressions of $q(t)$ are shown as follows:

$$\begin{aligned} q(t)=&\sum_{j=1}^{\infty}k_{ij}\omega_{coj}e^{-\omega_{coj}}\left(1-\frac{\omega_{coj}}{\sqrt{\omega_{coj}^2-\omega_{hj}^2}}\right)e^{\sqrt{\omega_{coj}^2-\omega_{hj}^2}t} \\ &+\sum_{j=1}^{\infty}k_{ij}\omega_{coj}e^{-\omega_{coj}}\left(1+\frac{\omega_{coj}}{\sqrt{\omega_{coj}^2-\omega_{hj}^2}}\right)e^{-\sqrt{\omega_{coj}^2-\omega_{hj}^2}t} \end{aligned} \tag{12}$$

$$Q(s)=\sum_{j=1}^{\infty}\frac{2k_{ij}\omega_{coj}s}{s^2+2\omega_{coj}s+\omega_{hj}^2} \tag{13}$$

where k_i is the integral gain of the quasi-resonant filter. ω_{co} is the cutoff frequency of the quasi-resonant filter. ω_h is the resonant frequency of the quasi-resonant filter.

According to (10)–(12), a periodic interference signal of a specific frequency can be provided with infinite gain by a quasi-resonant filter. Therefore, zero static error tracking or interference suppression can be achieved at interference frequencies. The resonance characteristics of the system are considered by MFQRFD-LESO, which means that the gain is increased at the interference frequency, so that the interference component at that frequency is accurately estimated. At the same time, the observer introduces a cutoff frequency ω_{co} based on the traditional resonant filter, so that a certain bandwidth range exists near the resonant frequency ω_h. In this way, the interference frequency has a certain robustness, and a certain deviation is allowed to exist. Even if the actual interference frequency is not completely consistent with the design frequency, the observer can effectively estimate periodic interferences. Multiple interference frequencies are considered in the system, and multiple quasi-resonant filters will be connected in parallel. Periodic disturbances of different frequencies in the system will be corresponding to different single-frequency quasi-resonant filters, thus forming the structural form of multi-frequency quasi-resonant filters. The amplitude and phase of each interference frequency component can be estimated simultaneously.

B. Generalized Linear Extension State Observer

Due to the fact that second-order T-LESO can only observe step interference without errors, there will be observation errors when there are ramp and acceleration interference components in the lumped interference of the control system. To avoid the problem of speed fluctuations caused by high-order interference components during the operation of the motor, the second-order T-LESO is extended to the fourth-order G-LESO to achieve error-free observation of ramp and acceleration interferences. The expression for G-LESO is as follows:

$$\begin{cases} \dot{v}_1 = v_2 - l_1(v_1 - x_1) + b_0 u_G \\ \dot{v}_2 = v_3 - l_2(v_1 - x_1) \\ \dot{v}_3 = v_4 - l_3(v_1 - x_1) \\ \dot{v}_4 = -l_4(v_1 - x_1) \end{cases} \tag{14}$$

where v_1, v_2, v_3, and v_4 are the state variables of y, f_s, $\dot{f}_s$, and $\ddot{f}_s$. l_1. l_2, l_3, and l_4 are the state feedback gains of G-LESO.

The frequency domain expression of (14) can be obtained by applying Laplace transform as follows:

$$\begin{cases} V_1(s) = \frac{b_0 s^3}{s^4+l_1 s^3+l_2 s^2+l_3 s+l_4} U_G(s) \\ \qquad + \frac{l_1 s^3+l_1 s^2+l_3 s+l_4}{s^4+l_1 s^3+l_2 s^2+l_3 s+l_4} Y(s) \\ V_2(s) = -\frac{b_0 l_2 s^2+b_0 l_3 s+b_0 l_4}{s^4+l_1 s^3+l_2 s^2+l_3 s+l_4} U_G(s) \\ \qquad + \frac{l_2 s^3+l_3 s^2+l_4 s}{s^4+l_1 s^3+l_2 s^2+l_3 s+l_4} Y(s) \\ V_3(s) = -\frac{b_0 l_3 s^2+b_0 l_4 s}{s^4+l_1 s^3+l_2 s^2+l_3 s+l_4} U_G(s) \\ \qquad + \frac{l_3 s^3+l_4 s^2}{s^4+l_1 s^3+l_2 s^2+l_3 s+l_4} Y(s) \\ V_4(s) = -\frac{b_0 l_4 s^2}{s^4+l_1 s^3+l_2 s^2+l_3 s+l_4} U_G(s) \\ \qquad + \frac{l_4 s^3}{s^4+l_1 s^3+l_2 s^2+l_3 s+l_4} Y(s) \end{cases} \tag{15}$$

where $V_1(s)$, $V_2(s)$, $U_G(s)$, and $Y(s)$ are the Laplace transforms of v_1, v_2, u_G, and y.

The characteristic polynomial of G-LESO is the denominator polynomial of (15), which associates the feedback gain coefficient of the state observer with ω_{o2} (ω_{o2} is the bandwidth of G-LESO).

$$s^4 + l_1 s^3 + l_2 s^2 + l_3 s + l_4 = (s + \omega_{o2})^4. \tag{16}$$

From (16), $l_1 = 4\omega_{o2}$, $l_2 = 6\omega_{o2}^2$, $l_3 = 4\omega_{o2}^3$, $l_4 = \omega_{o2}^4$.

C. Design of Speed Loop Controller for IPMSM Drive System Based on I-LADRC

The speed fluctuation problem caused by periodic and aperiodic interferences in IPMSM control systems is mainly addressed in this article, especially the impact of periodic and high-order interferences. Therefore, an I-LADRC in which MFQRFD-LESO and G-LESO are cascaded is proposed. At this point, the MFQRFD-LESO is used as the first-level LESO, the G-LESO is used as the second-level LESO, and the interference observed by MFQRFD-LESO is used as the known interference component of G-LESO. The expression is as follows:

$$\begin{cases} \dot{z}_1 = z_2 + b_0 u_I \\ \underbrace{\dot{z}_2 = -(2\omega_{o1} + q(t))(\dot{z}_1 - \dot{x}_1) - \omega_{o1}^2(z_1 - x_1)}_{\text{MFQRFD-LESO}} \\ \dot{v}_1 = v_2 + z_2 - 4\omega_{o2}(v_1 - x_1) + b_0 u_I \\ \dot{v}_2 = v_3 - 6\omega_{o2}^2(v_1 - x_1) \\ \dot{v}_3 = v_4 - 4\omega_{o2}^3(v_1 - x_1) \\ \underbrace{\dot{v}_4 = -\omega_{o2}^4(v_1 - x_1)}_{\text{G-LESO}} \\ u_I = \frac{\omega_c(r - z_1) - (z_2 + v_2)}{b_0} \end{cases} . \tag{17}$$

According to (17), the outer loop controller of the IPMSM control system based on I-LADRC is shown as follows:

$$\begin{cases} \dot{\hat{\omega}}_{m1} = \hat{f}_{s1} + \frac{1}{\tilde{J}} T_e^* \\ \underbrace{\dot{\hat{f}}_{s1} = -(2\omega_{o1} + q(t))(\dot{\hat{\omega}}_{m1} - \dot{\omega}_{m1}) - \omega_{o1}^2(\hat{\omega}_{m1} - \omega_m)}_{\text{MFQRFD-LESO}} \\ \dot{\hat{\omega}}_{m1} = \hat{f}_{s2} + \hat{f}_{s1} - 4\omega_{o2}(\hat{\omega}_{m2} - \omega_m) + \frac{1}{\tilde{J}} T_e^* \\ \dot{\hat{f}}_{s2} = \hat{\hat{f}}_{s2} - 6\omega_{o2}^2(\hat{\omega}_{m2} - \omega_m) \\ \dot{\hat{\hat{f}}}_{s2} = \hat{\hat{f}}_{s2} - 4\omega_{o2}^3(\hat{\omega}_{m2} - \omega_m) \\ \underbrace{\dot{\hat{\hat{f}}}_{s2} = -\omega_{o2}^4(\hat{\omega}_{m2} - \omega_m)}_{\text{G-LESO}} \\ T_e^* = \frac{\omega_c(\omega_m^* - \hat{\omega}_{m1}) - (\hat{f}_{s1} + \hat{f}_{s2})}{1/\tilde{J}} \end{cases} \tag{18}$$

where $\hat{\omega}_{m1}$ and $\hat{\omega}_{m2}$ are the observed rotational speeds of MFQRFD-LESO and G-LESO. f_{s1} and f_{s2} are the interferences observed by MFQRFD-LESO and G-LESO, and $f_s = f_{s1} + f_{s2}$.

According to (18), the control block diagram of the IPMSM control system based on I-LADRC is shown in Fig. 3. The structural diagram of the cascade of MFQRFD-LESO and G-LESO is shown in Fig. 4.

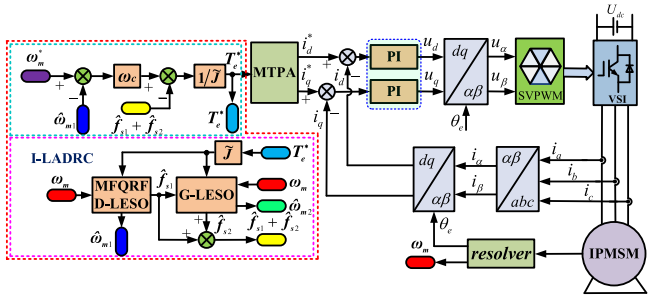

Fig. 3. Control block diagram of IPMSM control system based on I-LADRC.

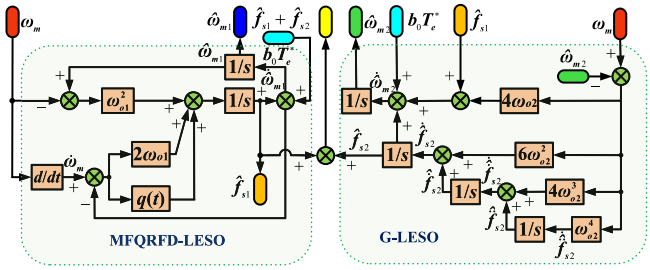

Fig. 4. Structure diagrams of MFQRFD-LESO and G-LESO are cascaded.

From Figs. 3 and 4, MFQRFD-LESO is mainly used to observe periodic interferences subjected by the system, while G-LESO is mainly used to observe high-order interferences subjected by the system.

IV. Performance Analysis of IPMSM Driver System Control Based on I-LADRC

The primary purpose of a control system is to ensure stable operation, and its essence is to resist interferences. First, the prerequisite assumptions for conducting control performance analysis are given in this section, and their rationality in practical applications is analyzed. Then, the stability of the IPMSM closed-loop system based on I-LADRC is demonstrated. Finally, the anti-interference characteristics of I-LADRC based on MFQRFD-LESO and the estimation performance of G-LESO are analyzed.

A. Preconditions and Assumptions

When the control performance of the IPMSM drive system based on I-LADRC is theoretically analyzed, the following assumptions need to be made regarding the input and output of the controller, the input and output of the extended state observer, and the lumped interference experienced by the system:

For the input r and output u of I-LADRC, as shown in (17), the r and its derivatives $\dot{r}, \ddot{r}, \ldots, r^{(n)}$, as well as the u, are all bounded functions with respect to time t, i.e., $|r(t)| \le \delta_0, |\dot{r}(t)| \le \delta_1, \ldots, |r^{(n)}(t)| \le \delta_n$, $|u| \le \varepsilon$. Where δ_0, δ_1, δ_n, and ε are all positive numbers. The input and output quantities in the abovementioned assumptions correspond to the given speed ω_m^* and torque T_e^*in the speed loop of the IPMSM drive system, respectively. The reason for making bounded assumptions about ω_m^* and T_e^* is that in practical engineering, they are subjected to amplitude limiting to ensure the accuracy and safety of the system.

For the input and output quantities of LESO (MFQRFD-LESO and G-LESO), taking MFQRFD-LESO as an example, the estimated aggregate interference f_{s1} is represented as the superposition of internal interference $\zeta_{s1}(x)$ and external interference $\vartheta_{s1}(t)$. Its expression is as follows:

$$f_{s1}(x,t,u) = \zeta_{s1}(x) + \vartheta_{s1}(t) \tag{19}$$

where $\zeta_s(x)$ is an unknown nonlinear function about the state variable x.

For first-order nonlinear uncertain systems containing $f_{s1}(x,t,u)$, the following assumptions must be met:

1) $f_{s1}(x,t,u)$ is continuously differentiable, and $\forall \phi \ge 0$, if $|x| \le \phi$, then

$$|f_{s1}(x,t,u)| \le \alpha(\phi), \ \left|\frac{\partial f_{s1}(x,t,u)}{\partial x}\right| \le \alpha(\phi) \tag{20}$$

where $\alpha(\cdot) : \mathbb{R}^+ \to \mathbb{R}^+$ is a known finite function.

2) $\vartheta_{s1}(t)$ is continuously differentiable and satisfies

$$|\vartheta(t)| \le c, \ \left|\dot{\vartheta}(t)\right| \le c, \ \forall t \ge t_0 \tag{21}$$

where $c > 0$ is a known constant.

For the uncertain nonlinear system (3) satisfying the two assumptions (a) and (b), for any given initial value ϕ_0 of the state variable, $\exists \omega_{o1}^* > 0$, as long as $\omega_{o1} > \omega_{o1}^*$, the closed-loop control system based on I-LADRC has the following properties:

$$|x_1(t) - x_1^*(t)| \le \frac{\chi_1^*}{\omega_{o1}}, \ t \ge t_0 \tag{22}$$

$$\left\| \begin{pmatrix} x_1(t) - z_1(t) \\ x_2(t) - z_2(t) \end{pmatrix} \right\| \le \frac{\chi_2^*}{\omega_{o1}} + \chi_3^* e^{-\chi_4^* \omega_{o1}(t-t_o)} \tag{23}$$

where ω_o^*, χ_1^*, χ_2^*, χ_3^*, and χ_4^* are positive numbers related to ϕ_0, $\alpha(\cdot)$,c, and ω_c.

For $x_1^*(t)$, it is the expected control process curve that satisfies the following dynamic process starting from the initial value $x_1(t_0)$:

$$\dot{x}_1^*(t) = -\omega_c x_1^*(t), \ x_1^*(t_0) = x_1(t_0) \tag{24}$$

where t_0 is the initial time.

In practical engineering applications, (22) reveals the existence of ω_{o1} and ω_c, which enable a family of nonlinear uncertain systems containing $f_{s1}(x,t,u)$ that satisfy the assumed conditions to be controlled. Therefore, the controlled variable $x_1(t)$ is not only bounded but also the error size between it and the expected dynamic process $x_1^*(t)$ can be adjusted by ω_o, while the dynamic quality of the system is adjusted by ω_c. The property of LESO's estimation error for aggregate interference can be revealed by (23), which not only reveals that the estimation error is bounded, but also that the size of the estimation error can be adjusted by ω_o. Therefore, the assumptions of LESO mentioned earlier are in line with practical engineering applications.

For the $\zeta_{s1}(x)$ and $\vartheta_{s1}(t)$ experienced by the system, where $\zeta_{s1}(x)$ is related to the system state variable x, it can be directly proven that $\zeta_{s1}(x)$ is bounded. Therefore, it cannot be assumed that $\zeta_{s1}(x)$ is bounded. For $\vartheta_{s1}(t)$, since it is only related to t, it is

directly assumed that $\vartheta_{s1}(t)$ and its derivatives of various orders are bounded, which meets the requirements of actual operating conditions.

B. Proof of Stability

The local stability of MFQRFD-LESO and G-LESO is first analyzed in this section, and then the stability of the IPMSM closed-loop system based on I-LADRC is demonstrated.

For the local stability of MFQRFD-LESO, to facilitate analysis, taking a single-frequency quasi-resonant filter as an example, the following equations can be obtained from (11):

$$\begin{cases} Z_1(s) = \frac{\varpi_{11}(s)}{\varsigma_{11}(s)}U(s) + \frac{\varpi_{12}(s)}{\varsigma_{12}(s)}Y(s) \\ Z_2(s) = \frac{\varpi_{21}(s)}{\varsigma_{21}(s)}U(s) + \frac{\varpi_{22}(s)}{\varsigma_{22}(s)}Y(s) \end{cases} \tag{25}$$

where $Z_1(s)$ and $Z_2(s)$ are the Laplace transforms of z_1 and z_2.

Let $\varsigma_{11}(s) = \varsigma_{12}(s) = \varsigma_{21}(s) = \varsigma_{22}(s) = \varsigma(s)$, its expressions are as follows:

$$\varsigma(s) = a_0 s^4 + a_1 s^3 + a_2 s^2 + a_3 s + a_4 \tag{26}$$

where $a_0 = 1$, $a_1 = 2\omega_{co} + 2\omega_{o1}$, $a_2 = \omega_h^2 + 4\omega_{co}\omega_{o1} + 2k_i\omega_{co} + \omega_{o1}^2$, $a_3 = 2\omega_{o1}\omega_h^2 + 2\omega_{o1}^2\omega_{co}$, $a_4 = \omega_{o1}^2\omega_h^2$.

For $\varpi_{11}(s)$, $\varpi_{12}(s)$, $\varpi_{21}(s)$, and $\varpi_{22}(s)$, their expressions are as follows:

$$\begin{cases} \varpi_{11}(s) = b_0 s^3 + 2b_0\omega_{co}s^2 + b_0\omega_h^2 s \\ \varpi_{12}(s) = 2\omega_{o1}s^3 + (4\omega_{o1}\omega_{co} + 2k_i\omega_{co} + \omega_{o1}^2)s^2 \\ \qquad + (2\omega_{o1}\omega_h^2 + 2\omega_{o1}^2\omega_{co})s + \omega_{o1}^2\omega_h^2 \\ \varpi_{21}(s) = 2b_0\omega_{o1}s^3 + (4b_0\omega_{o1}\omega_{co} + 2b_0k_i\omega_{co} + b_0\omega_{o1}^2)s^2 \\ \qquad + (2b_0\omega_{o1}\omega_h^2 + 2b_0\omega_{o1}^2\omega_{co})s + b_0\omega_{o1}^2\omega_h^2 \\ \varpi_{22}(s) = 2\omega_{o1}s^4 + (4\omega_{o1}\omega_{co} + 2k_i\omega_{co})s^3 \\ \qquad + (2\omega_{o1}\omega_h^2 + 2\omega_{o1}^2\omega_{co})s^2 + \omega_{o1}^2\omega_h^2 s \end{cases} . \tag{27}$$

For (27), ω_{co}, ω_{o1}, ω_h, and k_i are all positive numbers, it is ensured that a_0, a_1, a_2, a_3, and a_4 are all positive numbers. According to the Linnard–Chipater stability criterion [33], the odd-order Hurwitz determinant is shown as follows:

$$\Delta_{MFQRFD1} = a_1 = 2\omega_{co} + 2\omega_{o1} > 0 \tag{28}$$

$$\begin{aligned} \Delta_{MFQRFD3} &= \begin{vmatrix} a_1 & a_3 & a_5 \\ a_0 & a_2 & a_4 \\ 0 & a_1 & a_3 \end{vmatrix} = a_1a_2a_3 + a_0a_1a_5 - a_0a_3^2 - a_1^2a_4 \\ &= 16\omega_{co}^3\omega_{o1}^3 + 8k_i\omega_{co}^3\omega_{o1}^2 + 16\omega_{co}^2\omega_h^2\omega_{o1}^2 \\ &\quad + 8k_i\omega_{co}^2\omega_h^2\omega_{o1} + 16\omega_{co}^2\omega_{o1}^4 + 8k_i\omega_{co}^2\omega_{o1}^3 \\ &\quad + 4\omega_{co}\omega_h^4\omega_{o1} + 8\omega_{co}\omega_h^2\omega_{o1}^3 + 8k_i\omega_{co}\omega_h^2\omega_{o1}^2 \\ &\quad + 4\omega_{co}\omega_{o1}^5 > 0. \end{aligned} \tag{29}$$

According to (28) and (29), the $\Delta_{\mathrm{MFQRFD1}}$ and $\Delta_{\mathrm{MFQRFD3}}$ are both positive numbers, indicating that MFQRFD-LESO is locally stable.

For G-LESO, it can be obtained from (15) and (16)

$$\begin{cases} V_1(s) = \frac{\tau_{11}(s)}{\upsilon_{11}(s)}U(s) + \frac{\tau_{12}(s)}{\upsilon_{12}(s)}Y(s) \\ V_2(s) = -\frac{\tau_{21}(s)}{\upsilon_{21}(s)}U(s) + \frac{\tau_{22}(s)}{\upsilon_{22}(s)}Y(s) \\ V_3(s) = -\frac{\tau_{31}(s)}{\upsilon_{31}(s)}U(s) + \frac{\tau_{32}(s)}{\upsilon_{32}(s)}Y(s) \\ V_4(s) = -\frac{\tau_{41}(s)}{\upsilon_{41}(s)}U(s) + \frac{\tau_{42}(s)}{\upsilon_{42}(s)}Y(s) \end{cases} . \tag{30}$$

Let $\upsilon_{11}(s) = \upsilon_{12}(s) = \cdots = \upsilon_{41}(s) = \upsilon_{42}(s) = \upsilon(s)$, its expressions are as follows:

$$\upsilon(s) = \mu_0 s^4 + \mu_1 s^3 + \mu_2 s^2 + \mu_3 s + \mu_4 \tag{31}$$

where$\mu_0 = 1$,$\mu_1 = 4\omega_{o2}$,$\mu_2 = 6\omega_{o2}^2$,$\mu_3 = 4\omega_{o2}^3$,$\mu_4 = \omega_{o2}^4$.

For $\tau_{11}(s)$, $\tau_{12}(s) \cdots \tau_{41}(s)$, and $\tau_{42}(s)$, their expressions are as follows:

$$\begin{cases} \tau_{11}(s) = b_0 s^3 \\ \tau_{12}(s) = 4\omega_{o2}s^3 + 6\omega_{o2}^2s^2 + 4\omega_{o2}^3s + \omega_{o2}^4 \\ \tau_{21}(s) = 6b_0\omega_{o2}^2 + 4b_0\omega_{o2}^3 + b_0\omega_{o2}^4 \\ \tau_{22}(s) = 6\omega_{o2}^2s^3 + 4\omega_{o2}^3s^2 + \omega_{o2}^4 s \\ \tau_{31}(s) = 4b_0\omega_{o2}^3s^2 + b_0\omega_{o2}^4 s \\ \tau_{32}(s) = 4\omega_{o2}^3s^3 + \omega_{o2}^4 s^2 \\ \tau_{41}(s) = b_0\omega_{o2}^4 s^2 \\ \tau_{42}(s) = \omega_{o2}^4 s^3 \end{cases} . \tag{32}$$

For the local stability of G-LESO, since ω_{o2} is a positive number, the coefficients of all order terms of the G-LESO characteristic polynomial are ensured to be positive numbers. According to the Linnard–Chipater stability criterion, the odd-order Hurwitz determinant is shown as follows:

$$\Delta_{G1} = \mu_1 = 4\omega_{o2} > 0 \tag{33}$$

$$\begin{aligned} \Delta_{G3} &= \begin{vmatrix} \mu_1 & \mu_3 & \mu_5 \\ \mu_0 & \mu_2 & \mu_4 \\ 0 & \mu_1 & \mu_3 \end{vmatrix} = \mu_1\mu_2\mu_3 + \mu_0\mu_1\mu_5 - \mu_0\mu_3^2 - \mu_1^2\mu_4 \\ &= 64\omega_{o2}^6 > 0. \end{aligned} \tag{34}$$

From (33) and (34), the Δ_{G1} and Δ_{G3} are both positive numbers, therefore, the G-LESO is locally stable.

Regarding the stability of closed-loop systems based on I-LADRC, the frequency domain expression of the system's output term $Y(s)$ based on the input term and interference term $F_s(s)$ can be obtained from (17) as follows:

$$\begin{cases} Y(s) = \frac{\omega_c}{s+\omega_c}R(s) + \frac{M(s)}{N(s)}F_s(s) \\ F_s(s) = F_{s1}(s) + F_{s2}(s) \end{cases} \tag{35}$$

where $R(s)$, $F_s(s)$, $F_{s1}(s)$, and $F_{s2}(s)$ are the Laplace transform of r, f_s, f_{s1}, and f_{s2}.

For (35), the expressions for $N(s)$ and $M(s)$ are as follows:

$$\begin{aligned} N(s) &= \alpha_0 s^9 + \alpha_1 s^8 + \alpha_2 s^7 + \alpha_3 s^6 + \alpha_4 s^5 \\ &\quad + \alpha_5 s^4 + \alpha_6 s^3 + \alpha_7 s^2 + \alpha_8 s + \alpha_9 \end{aligned} \tag{36}$$

$$\begin{aligned} M(s) &= \eta_0 s^8 + \eta_1 s^7 + \eta_2 s^6 + \eta_3 s^5 \\ &\quad + \eta_4 s^4 + \eta_5 s^3 + \eta_6 s^2 + \eta_7 s \end{aligned} \tag{37}$$

where

$$\alpha_0 = 1,\ \alpha_1 = 2\omega_{o1} + 4\omega_{o2} + \omega_c + 2\omega_{co},$$

$$\begin{aligned}\alpha_2 &= \omega_h^2 + 2\omega_c\omega_{co} + 8\omega_{o2}\omega_{co} + 2k_i\omega_{co} + 4\omega_{o2}\omega_c + 2\omega_{o1}\omega_c \\ &\quad + 6\omega_{o2}^2 + 8\omega_{o1}\omega_{o2} + 4\omega_{o1}\omega_{co} + \omega_{o1}^2,\end{aligned}$$

$$\begin{aligned}\alpha_3 &= 2\omega_{o1}\omega_h^2 + 2\omega_{o1}^2\omega_{co} + 4\omega_{o2}\omega_h^2 + 16\omega_{o1}\omega_{o2}\omega_{co} \\ &\quad + 8k_i\omega_{o2}\omega_{co} + 4\omega_{o1}^2\omega_{o2} + \omega_c\omega_h^2 + 4\omega_c\omega_{o1}\omega_{co} \\ &\quad + 2k_i\omega_c\omega_{co} + \omega_c\omega_{o1}^2 + 8\omega_{o2}\omega_c\omega_{co} + 8\omega_{o1}\omega_{o2}\omega_c \\ &\quad + 12\omega_{o2}^2\omega_{co} + 12\omega_{o1}\omega_{o2}^2 + 6\omega_{o2}^2\omega_c + 4\omega_{o2}^3,\end{aligned}$$

$$\begin{aligned}\alpha_4 &= 4\omega_{o2}\omega_c\omega_h^2 + 2\omega_{o1}\omega_c\omega_h^2 + 6\omega_{o2}^2\omega_h^2 \\ &\quad + 8\omega_{o1}\omega_{o2}\omega_h^2 + \omega_{o1}^2\omega_h^2 \\ &\quad + 12\omega_{o2}^2\omega_c\omega_{co} + 16\omega_{o1}\omega_{o2}\omega_c\omega_{co} \\ &\quad + 8k_i\omega_{o2}\omega_c\omega_{co} + 2\omega_{o1}^2\omega_c\omega_{co} \\ &\quad + 8\omega_{o2}^3\omega_{co} + 24\omega_{o1}\omega_{o2}^2\omega_{co} + 12k_i\omega_{o2}^2\omega_{co} \\ &\quad + 8\omega_{o1}^2\omega_{o2}\omega_{co} + \omega_{o2}^4 \\ &\quad + 8\omega_{o2}^3\omega_{o1} + 6\omega_{o1}^2\omega_{o2}^2 + 4\omega_{o2}^3\omega_c + 12\omega_{o1}\omega_{o2}^2\omega_c \\ &\quad + 4\omega_{o1}^2\omega_{o2}\omega_c,\end{aligned}$$

$$\begin{aligned}\alpha_5 &= 6\omega_{o2}^2\omega_c\omega_h^2 + 8\omega_{o1}\omega_{o2}\omega_c\omega_h^2 + \omega_{o1}^2\omega_c\omega_h^2 + 4\omega_{o2}^3\omega_h^2 \\ &\quad + 12\omega_{o1}\omega_{o2}^2\omega_h^2 + 4\omega_{o1}^2\omega_{o2}\omega_h^2 + 2\omega_{o2}^4\omega_{co} + 16\omega_{o1}\omega_{o2}^3\omega_{co} \\ &\quad + 8k_i\omega_{o2}^3\omega_{co} + 12\omega_{o1}^2\omega_{o2}^2\omega_{co} + 8\omega_{o2}^3\omega_c\omega_{co} \\ &\quad + 24\omega_{o1}\omega_{o2}^2\omega_c\omega_{co} \\ &\quad + 12k_i\omega_{o2}^2\omega_c\omega_{co} + 8\omega_{o1}^2\omega_{o2}\omega_c\omega_{co} + 2\omega_{o1}\omega_{o2}^4 + 4\omega_{o1}^2\omega_{o2}^3 \\ &\quad + \omega_{o2}^4\omega_c + 8\omega_{o1}\omega_{o2}^3\omega_c + 6\omega_{o1}^2\omega_{o2}^2\omega_c,\end{aligned}$$

$$\begin{aligned}\alpha_6 &= \omega_{o2}^4\omega_h^2 + 8\omega_{o1}\omega_{o2}^3\omega_h^2 + 6\omega_{o1}^2\omega_{o2}^2\omega_h^2 + 4\omega_{o2}^3\omega_c\omega_h^2 \\ &\quad + 12\omega_{o1}\omega_{o2}^2\omega_c\omega_h^2 + 8\omega_{o1}^2\omega_{o2}^3\omega_{co} + 2\omega_{o2}^4\omega_c\omega_{co} \\ &\quad + 4\omega_c\omega_{o1}^2\omega_{o2}\omega_h^2 + 4\omega_{o1}\omega_{o2}^4\omega_{co} + 2k_i\omega_{o2}^4\omega_{co} \\ &\quad + 16\omega_{o1}\omega_{o2}^3\omega_c\omega_{co} + 8k_i\omega_{o2}^3\omega_c\omega_{co} + 12\omega_{o1}^2\omega_{o2}^2\omega_c\omega_{co} \\ &\quad + \omega_{o1}^2\omega_{o2}^4 + 2\omega_{o1}\omega_{o2}^4\omega_c + 4\omega_{o1}^2\omega_{o2}^3\omega_c,\end{aligned}$$

$$\begin{aligned}\alpha_7 &= 2\omega_h^2\omega_{o1}\omega_{o2}^4 + 4\omega_{o1}^2\omega_{o2}^3\omega_h^2 + \omega_{o2}^4\omega_c\omega_h^2 + 8\omega_{o1}\omega_{o2}^3\omega_c\omega_h^2 \\ &\quad + 6\omega_{o1}^2\omega_{o2}^2\omega_c\omega_h^2 + \omega_{o1}^2\omega_{o2}^4\omega_c + 2\omega_{o1}^2\omega_{o2}^4\omega_{co} \\ &\quad + 4\omega_{o1}\omega_{o2}^4\omega_c\omega_{co} + 2k_i\omega_{o2}^4\omega_c\omega_{co} + 8\omega_{o1}^2\omega_{o2}^3\omega_c\omega_{co},\end{aligned}$$

$$\begin{aligned}\alpha_8 &= \omega_{o1}^2\omega_{o2}^4\omega_h^2 + 2\omega_{o1}^2\omega_{o2}^4\omega_c\omega_{co} + 2\omega_{o1}\omega_{o2}^4\omega_c\omega_h^2 \\ &\quad + 4\omega_{o1}^2\omega_{o2}^3\omega_c\omega_h^2,\end{aligned}$$

$$\alpha_9 = \omega_{o1}^2\omega_{o2}^4\omega_c\omega_h^2.$$

$$\eta_0 = 1,\ \eta_1 = 2\omega_{co} + \omega_c + 4\omega_{o2},$$

$$\eta_2 = \omega_h^2 + 2\omega_c\omega_{co} + 8\omega_{o2}\omega_{co} + 4\omega_{o2}\omega_c,$$

$$\eta_3 = \omega_c\omega_h^2 + 4\omega_{o2}\omega_h^2 + 8\omega_{o2}\omega_c\omega_{co} + 6\omega_{o2}^2\omega_c,$$

$$\eta_4 = 4\omega_{o2}\omega_c\omega_h^2 + 12\omega_{o2}^2\omega_c\omega_{co} + 4\omega_{o2}^3\omega_c,$$

$$\eta_5 = 6\omega_{o2}^2\omega_c\omega_h^2 + 8\omega_{o2}^3\omega_c\omega_{co} + \omega_{o2}^4\omega_c,$$

$$\eta_6 = 4\omega_{o2}^3\omega_c\omega_h^2 + 2\omega_{o2}^4\omega_c\omega_{co},\ \eta_7 = \omega_{o2}^4\omega_c\omega_h^2.$$

According to (35), the closed-loop pole of the transfer function based on the input term is $s = -\omega_c$. Therefore, the system is stable. For the transfer function of the system output term based on the interference term, it can be obtained from (36) that the coefficients α_0, α_1, ⋯, α_8, and α_9 of the characteristic polynomial of each order are all positive numbers. Meanwhile, its Hurwitz determinant is shown as follows:

$$\Delta_n = \begin{vmatrix} \alpha_1 & \alpha_3 & \alpha_5 & \dots & \alpha_{2n-1} \\ \alpha_0 & \alpha_2 & \alpha_4 & \dots & \alpha_{2n-2} \\ 0 & \alpha_1 & \alpha_3 & \dots & \alpha_{2n-3} \\ 0 & \alpha_0 & \alpha_2 & \dots & \alpha_{2n-4} \\ \vdots & \vdots & \vdots & \ddots & \vdots \\ 0 & 0 & 0 & \dots & \alpha_n \end{vmatrix}. \tag{38}$$

For (38), according to the Linnard–Chipater stability criterion, the odd-order Hurwitz determinants Δ_1, Δ_3, Δ_5, Δ_7, and Δ_9 are all positive numbers. The IPMSM control system based on I-LADRC is a stable system.

C. Analysis of Anti-Interference Characteristics

Regarding the observation ability of MFQRFD-LESO for periodic interferences. The transfer function of the output term of LADRC with MFQRFD-LESO (MFQRFD-LADRC) for interference term can be obtained from (9)

$$\Phi_{MFQRFD}(s) = \frac{Y(s)}{F_s(s)} = \frac{s}{\rho_0 s^4 + \rho_1 s^3 + \rho_2 s^2 + \rho_3 s + \rho_4} \tag{39}$$

where $\rho_0 = 1, \rho_1 = 2\omega_{o2} + 2\omega_{co}, \rho_2 = 4\omega_{o2}\omega_{co} + 2k_i\omega_{co} + \omega_{o2}^2 + \omega_h^2, \rho_3 = 2\omega_{o2}^2\omega_{co} + 2\omega_{o2}\omega_h^2, \rho_4 = \omega_{o2}^2\omega_h^2$.

According to (39), the parameters ω_{o2}, ω_{co}, k_i, and ω_h are related to the parameter of $\Phi_{\mathrm{MFQRFD}}(s)$. Therefore, the Bode plot of $\Phi_{\mathrm{MFQRFD}}(s)$ with different parameter variations can be obtained as shown in Fig. 5.

The Bode plot of the T-LADRC output term based on the perturbation term is also shown in Fig. 5. For Fig. 5(a), with the increase of ω_{o1}, its capability to suppress low-frequency interference is enhanced, while the interference suppression capability of medium and high frequencies remains unchanged. For Fig. 5(b), with the increase of K_i, its capability to suppress mid-frequency interference is enhanced, while its anti-interference ability in the low- and high-frequency bands remains unchanged. For Fig. 5(c), with the increase of ω_{co}, its anti-interference ability in the full frequency range remains basically unchanged. For Fig. 5(d), with the change of ω_h, periodic interferences of different frequencies can be effectively suppressed. It can be concluded that I-LADRC can not only suppress periodic interferences in the system but also has better interference compensation capability than T-LADRC in the low to medium frequency range under the same ω_o conditions.

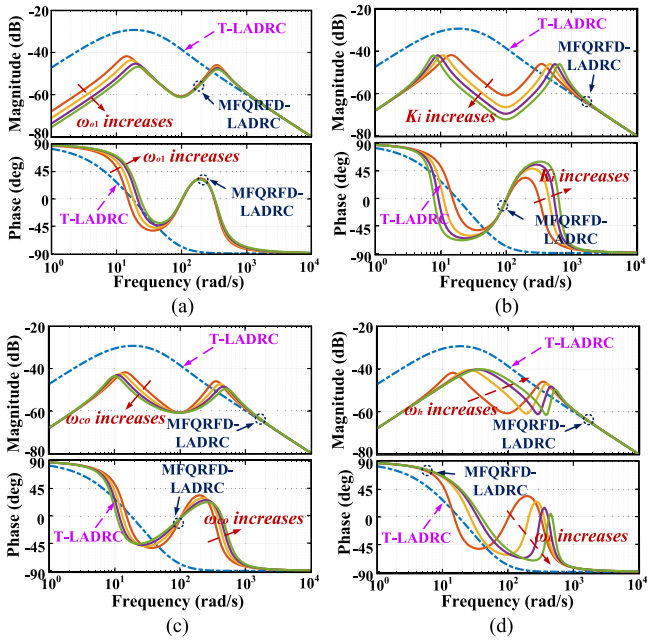

Fig. 5. Bode plot of $\Phi_{\mathrm{MFQRFD}}(s)$ as different parameters change. (a) When ω_{o2} changes. (b) When k_i changes. (c) When ω_{co} changes. (d) When ω_h changes.

D. Analysis of Estimated Characteristics

Regarding the estimation performance of G-LESO for disturbances of different orders, the observed interference value of G-LESO based on $G_{\mathrm{G}}(s)$ of the actual interference value and $\Xi_{\mathrm{G}}(s)$ of the interference observation error can be obtained from (15), (16), and $sY(s) = F_s(s) + b_0U(s)$ (where $sY(s) = F_s(s) + b_0U(s)$ is the Laplace transform of $\dot{y} = f_s(x,t,u) + b_0u$), as follows:

$$G_G(s) = \frac{V_2(s)}{F_{s2}(s)} = \frac{6\omega_o^2 s^2 + 4\omega_o^3 s + \omega_o^4}{s^4 + 4\omega_o s^3 + 6\omega_o^2 s^2 + 4\omega_o^3 s + \omega_o^4} \tag{40}$$

$$\Xi_G(s) = \frac{V_2(s) - F_{s2}(s)}{F_{s2}(s)} = \frac{s^4 + 4\omega_o s^3}{s^4 + 4\omega_o s^3 + 6\omega_o^2 s^2 + 4\omega_o^3 s + \omega_o^4}. \tag{41}$$

For the convenience of comparison and analysis with other observers, the observer bandwidth in $G_{\mathrm{G}}(s)$ and $\Xi_{\mathrm{G}}(s)$ is also represented by ω_o.

For the three-order disturbance differential compensation linear extended state observer (DDC-LESO), the observed interference value of DDC-LESO can be obtained from [34] based on $G_{\mathrm{DDC}}(s)$ of the actual interference value and $\Xi_{\mathrm{DDC}}(s)$ of the interference observation error, as follows:

$$G_{DDC}(s) = \frac{3\omega_o^2 s + \omega_o^3}{s^3 + 3\omega_o s^2 + 3\omega_o^2 s + \omega_o^3} \tag{42}$$

$$\Xi_{DDC}(s) = \frac{s^3 + 3\omega_o s^2}{s^3 + 3\omega_o s^2 + 3\omega_o^2 s + \omega_o^3}. \tag{43}$$

According to (5) and (6), the observed interference value of T-LESO is based on $G_{\mathrm{T}}(s)$ of the actual interference value and

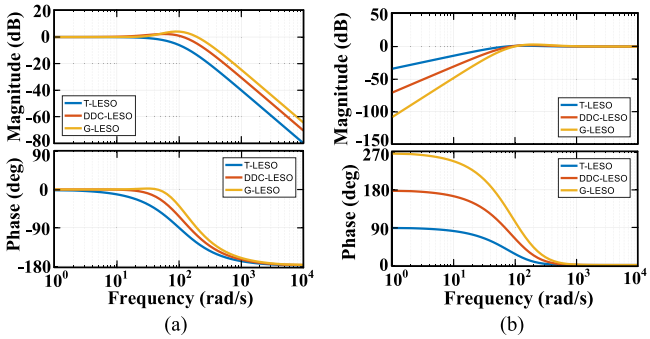

Fig. 6. Bode plots of lumped interference observations for G-LESO, DDC-LESO, and T-LESO based on actual lumped interference values and lumped interference observation errors. (a) Bode plots of lumped interference observed based on actual lumped interference values. (b) Bode plots of lumped interference observations based on lumped interference observation errors.

$\Xi_{\mathrm{T}}(s)$ of the interference observation error as follows:

$$G_T(s) = \frac{\omega_o^2}{s^2 + 2\omega_o s + \omega_o^2} \tag{44}$$

$$\Xi_T(s) = \frac{s^2 + 2\omega_o s}{s^2 + 2\omega_o s + \omega_o^2}. \tag{45}$$

From (40)–(45), the G(s) and $\Xi(s)$ of G-LESO, DDC-LESO, and T-LESO are only related to ω_o. The Bode plots of G(s) and $\Xi(s)$ for the three observers under the same ω_o conditions can be obtained, as shown in Fig. 6.

From Fig. 6(a), when ω_o is taken to the same value, compared to DDC-LESO and T-LESO, the observation accuracy of G-LESO for the lumped interference is improved at the same interference frequency. Under the same interference amplitude conditions, the observation range of G-LESO for the lumped interference is expanded. As a result, the high-frequency oscillation problem caused by increasing ω_o is avoided, and the impact of phase lag on the system is also reduced. Meanwhile, from Fig. 6(b), under the same conditions of ω_o, the observation error amplitude of G-LESO for low-frequency interferences is smaller than that of DDC-LESO and T-LESO. This indicates that G-LESO has strong low-frequency interference suppression capability.

When $f_{s2}(t)$ are the K_s, K_rt, and K_at^2, respectively, the time-domain expressions of G-LESO, DDC-LESO, and T-LESO for different interference observation errors can be obtained from (41), (43), and (45) as follows:

$$\begin{cases} \varepsilon_{sT}(t) = K_s e^{-\omega_o t} + K_s\omega_o t e^{-\omega_o t} \\ \varepsilon_{sDDC}(t) = K_s e^{-\omega_{os} t} + K_s\omega_o t e^{-\omega_{os} t} - K_s\omega_o^2 t^2 e^{-\omega_{os} t} \\ \varepsilon_{sG}(t) = K_s e^{-\omega_{os} t} + K_s t\omega_o e^{-\omega_{os} t} - 2.5K_s t^2\omega_o^2 e^{-\omega_{os} t} \\ \qquad\quad + 0.5K_s t^3\omega_o^3 e^{-\omega_{os} t} \end{cases} \tag{46}$$

$$\begin{cases} \varepsilon_{rT}(t) = 2K_r\omega_o^{-1} - 2K_r\omega_o^{-1} e^{-\omega_o t} - K_r t e^{-\omega_o t} \\ \varepsilon_{rDDC}(t) = K_r t e^{-\omega_o t} + K_r\omega_o t^2 e^{-\omega_o t} \\ \varepsilon_{rG}(t) = K_r t e^{-\omega_o t} - 0.5K_r t^3\omega_o^2 e^{-\omega_o t} + K_r t^2\omega_o e^{-\omega_o t} \end{cases} \tag{47}$$

TABLE I
OBSERVATION ERRORS OF G-LESO, DDC-LESO, AND T-LESO RELATIVE TO DIFFERENT INTERFERENCES

$\varepsilon \vert f_{s2}(t)$	K_s	$K_r t$	$K_a t^2$
ε_{G}	0	0	0
$\varepsilon_{\mathrm{DDC}}$	0	0	$3K_a/\omega_o^3$
ε_{T}	0	$2K_r/\omega_o$	∞

$$\begin{cases} \varepsilon_{aT}(t) = -3K_a\omega_o^{-2} + 2K_a\omega_o^{-1}t + 3K_a\omega_o^{-2}e^{-\omega_o t} \\ \qquad\quad + K_a\omega_o^{-1}te^{-\omega_o t} \\ \varepsilon_{aDDC}(t) = 3\omega_o^{-2} - 3K_a\omega_o^{-2}e^{-\omega_o t} - 3K_a\omega_o^{-1}te^{-\omega_o t} \\ \qquad\quad - K_a t^2 e^{-\omega_o t} \\ \varepsilon_{aG}(t) = 0.5K_a t^2 e^{-\omega_o t} + 0.5K_a t^3\omega_o e^{-\omega_o t} \end{cases} . \tag{48}$$

From (46)–(48), the observation errors of G-LESO, DDC-LESO, and T-LESO based on three different interferences are shown in Table I.

From Table I, T-LESO can only make effective estimates for step interferences. The DDC-LESO has zero observation errors for step and slope interferences, while G-LESO has zero observation errors for three different interferences. The G-LESO has better observation ability for high-order interferences compared to DDC-LESO and T-LESO.

From (46)–(48), the surface plots of G-LESO, DDC-LESO, and T-LESO with respect to three different interferences as they vary with ω_o and t are shown in Fig. 7.

From Fig. 7, it can be concluded that within a finite time, the observation errors of the three observers for step interferences are all zero, and compared to DDC-LESO and T-LESO, step interferences can be quickly converged by G-LESO. For ramp interferences, T-LESO has observation errors, while G-LESO and DDC-LESO can effectively converge to zero. For acceleration interferences, they can only be effectively converged by G-LESO. This further proves that G-LESO has better observational performance for acceleration interferences compared to DDC-LESO and T-LESO.

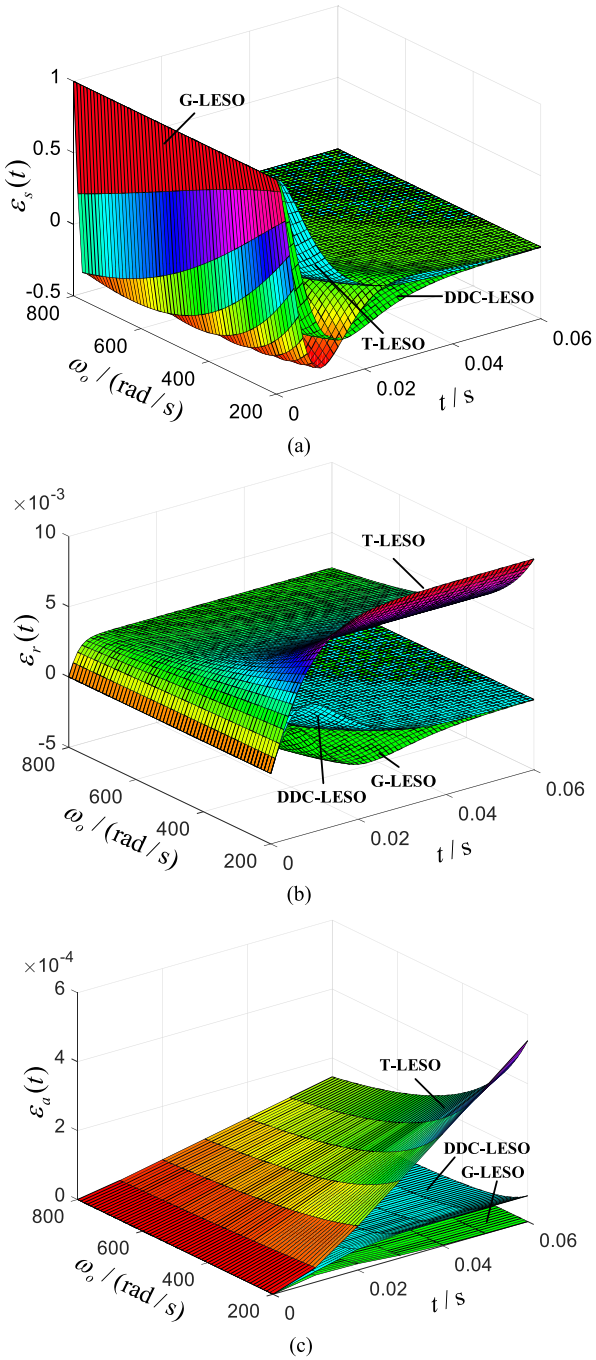

Fig. 7. G-LESO, DDC-LESO, and T-LESO surface plots for different interferences as ω_o and t vary. (a) Step interference. (b) Ramp interference. (c) Acceleration interference.

V. PARAMETER TUNING OF SPEED LOOP CONTROLLER FOR IPMSM DRIVE SYSTEM BASED ON I-LADRC

When conducting LADRC design and parameter tuning, the first step is to clarify the order of LADRC, that is, the selection of LADRC order should match the order of the controlled object. According to (1), the motion equation of IPMSM is a first-order differential equation, so first-order LADRC is used to control it. The reason why controllers with the same order as the system are adopted is mainly determined by the number of selected state variables in the system. For G-LESO, although the introduction of interference differential compensation signals expands LESO from the original second order to fourth order, the lumped interference differential is only used to generate early correction signals and is not fed back to the feedforward control end. Therefore, LSEF is still controlled by first-order feedforward. For MFQRFD-LESO, according to (11) and (12), after introducing a multifrequency quasi-resonant filter, three parameters, k_{ij}, ω_{coj}, and ω_{hj}, are added. Based on the abovementioned analysis and combined with (18), there are a total of seven parameters that need to be adjusted in the speed loop controller of the IPMSM drive system based on I-LADRC: ω_{o1}, ω_{o2}, ω_c, b_0, k_{ij}, ω_{coj}, and ω_{hj}.

For b_0, due to the impact caused by inertial mismatch systems that need to be considered in this article, b_0 is configured as the reciprocal of the nominal value of rotational inertia $\tilde{J}$, that is: $b_0 = 1/\tilde{J}$.

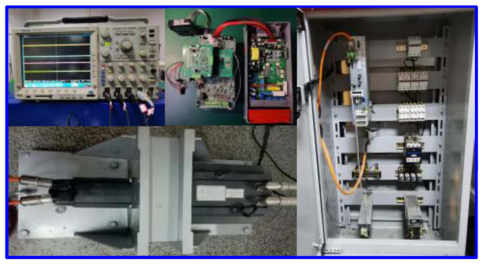

Fig. 8. 2 kW IPMSM docking physics experimental platform.

For ω_c, according to [35], the controller bandwidth frequency ω_c of the speed loop of the IPMSM drive system is usually set to 1/10 of the current loop bandwidth frequency ω_{cdq}, i.e., $\omega_c = \omega_{cdq}/10$. Based on the relationship between ω_c, ω_{cdq}, and time delay, ω_{cdq} is usually set to 1/20 of the carrier frequency f_c, i.e., $\omega_{cdq} = f_c/20$, therefore, $\omega_c = f_c/200$.

For ω_{o1} and ω_{o2}, the lumped interferences f_{s1} and f_{s2} estimated by MFQRFD-LESO and G-LESO are stacked together in a cascaded manner and then compensated by the same LSEF feedback. Therefore, ω_{o1} and ω_{o2} can be taken as the same value, that is, $\omega_{o1} = \omega_{o2}$. According to [36], there is a theoretical relationship of $\omega_o = (3 \sim 5)\omega_c$ between ω_c and ω_o (in practical engineering, it is the relationship of $\omega_o = (2 \sim 10)\omega_c$). In addition, digital control systems are limited by discrete-time delay characteristics, ω_{o1} and ω_{o2} must be less than $2/T_s$(where T_s is the sampling time). From this, the range of values for ω_{o1} and ω_{o2} can be determined, and after repeated debugging, the optimal values for ω_{o1} and ω_{o2} can be obtained to achieve the best performance of the IPMSM driving system.

For k_{ij}, ω_{coj}, and ω_{hj} ($j = 1,\ 2,\ 3,\ \ldots$), according to [37], $k_{ij} = 300j$, $\omega_{coj} = 1.5\%\omega_{hj}$, $\omega_{hj} = j\omega_e$. Among them, the resonant frequency ω_{hj} varies with the feedback angular velocity ω_e.

VI. Experiment Validation

To verify that the control performance of the control method proposed in this article is superior to T-LADRC and the QPR+DDC-ADRC proposed in [38], a 2 kW IPMSM vector control experimental platform is built as shown in Fig. 8. The hardware architecture diagram of the IPMSM driver system based on DSP digital implementation is shown in Fig. 9. The algorithm flowchart of the IPMSM driving system based on I-LADRC is shown in Fig. 10. The partial parameters of the IPMSM are shown in Table II.

To ensure fairness based on the comparison of three different controllers, I-LADRC, QPR+DDC-LADRC, and T-LADRC are compared and analyzed under the same conditions of ω_c, ω_o, and b_0 according to the parameter tuning principles provided in Section V. The specific parameter values are: $\omega_c = 20rad/s$,$\omega_o = 100rad/s$,$b_0 = 91(kg \cdot m^2)^{-1}$.

From Figs. 8 and 9, the system mainly consists of a main circuit, a control circuit IPMSM, composed of servo loading system and oscilloscope. The controlled motor is a three-phase IPMSM model 196STD-2C10D-X produced by Hongda Motor Co., Ltd., Liyang, China. The loading motor is a servo motor produced by Bosch Rexroth in Germany, with the model MSK050C-0600-NN-S1-UGO-NNNN. The core processor of the system is the TMS320F28335 chip from TI company. In

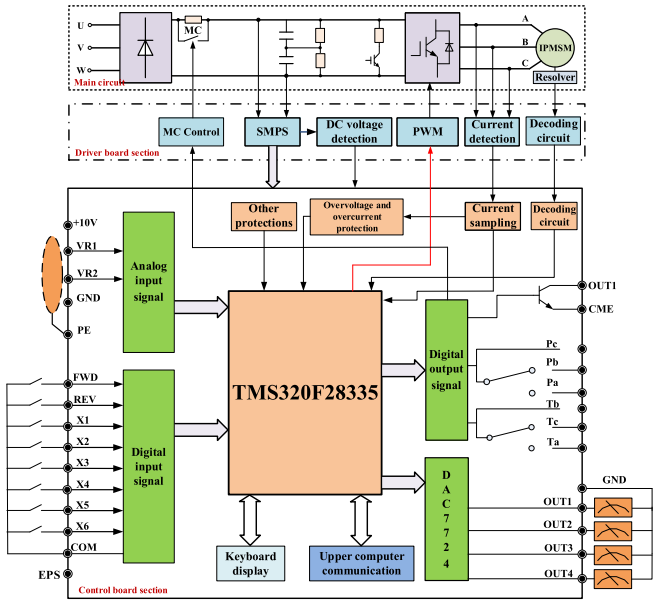

Fig. 9. Hardware architecture diagram of IPMSM driver system based on DSP digital implementation.

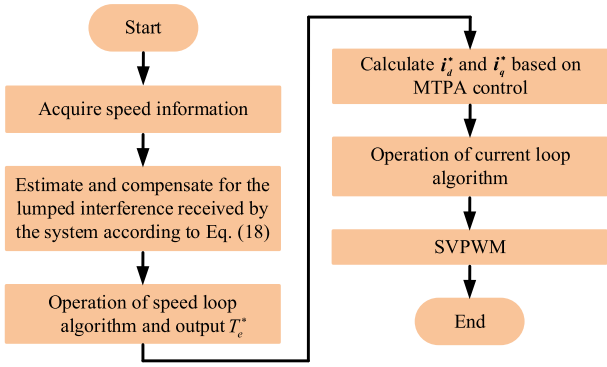

Fig. 10. Algorithm flowchart of the IPMSM driving system based on I-LADRC.

TABLE II
Experimental Parameters of IPMSM

Parameter	Value
Rated power	2 kW
Rated voltage	380 V
Rated current	5.8 A
Rated speed	1000 rpm
Rated frequency	66.67 Hz
Switching frequency	4 kHz
d-axis inductance	0.01085 H
q-axis inductance	0.02552 H
Moment of inertia	0.011 kg·m^2
Stator resistance	1.351 Ω
Permanent magnet flux linkage	0.77 Wb

the main circuit section, an ac–dc–ac topology circuit structure is adopted. By inputting 380 V three-phase ac power, it is then passed through a diode uncontrolled rectifier, and the rectified voltage is filtered by a large capacitor to obtain the dc bus voltage. Finally, through a three-phase bridge inverter circuit, the frequency-adjustable ac power is obtained to drive the IPMSM. In the driving circuit section, it mainly includes switch power supply, pulse driving signal, voltage detection circuit, and current detection circuit. In the control circuit section, it mainly consists of current sampling circuit, power device drive generation circuit, keyboard interface circuit, DA conversion circuit, analog and digital signal input and output circuit, overvoltage protection, overcurrent protection, and other protection circuits, as well as upper computer communication circuit. Meanwhile, the J52XFDW9754 rotary transformer is installed at the end of the IPMSM rotor shaft to obtain the actual rotor position and speed of the motor. The decoding board of the rotary transformer is processed by the AD2S1210 chip to decode the speed and position. The conversion of physical variables in the motor into graphical output is implemented by the DAC7724 chip in the smallest system board. The starting and stopping of the motor, control mode, and adjustment of control parameters are determined by the keyboard.

A. Characteristics of No-Load Speed

To verify that I-LADRC has better no-load speed characteristics compared to QPR+DDC-LADRC and T-LADRC. The waveforms of the given speed n^* and actual speed n of IPMSM when accelerating from stop to rated speed under no-load conditions are shown in Fig. 11. The multispeed waveform under no-load conditions is shown in Fig. 12.

From Fig. 11, for T-LADRC, the overshoot of n when accelerating to the steady-state value is 6%. For QPR+DDC-LADRC, the overshoot of n when accelerating to the steady-state value is 2.5%. For I-LADRC, there is no overshoot of n. From Fig. 12, when the speed changes, the motor will experience slight overshoot during acceleration when controlled by T-LADRC and QPR+DDC-LADRC, while the motor controlled by I-LADRC has no overshoot during acceleration at different speeds. This indicates that I-LADRC has better dynamic characteristics of no-load speed compared to T-LADRC and QPR+DDC-LADRC.

B. Verification of Anti-Interference Performance

To verify that the I-LADRC can suppress speed fluctuations caused by periodic interferences, when the system is injected with periodic interferences, under no-load conditions, the waveforms of the $n*$ and n of IPMSM during steady-state operation are shown in Fig. 13.

From Fig. 13, when controlled by T-LADRC, the fluctuation amplitude of the actual speed changes significantly. When controlled by QPR+DDC-LADRC, the fluctuation amplitude of the actual speed is slightly smaller than when T-LADRC is used. When controlled by I-LADRC, the fluctuation amplitude of the actual speed changes relatively little. This indicates that I-LADRC can suppress speed fluctuations caused by periodic interferences compared to T-LADRC and QPR+DDC-LADRC.

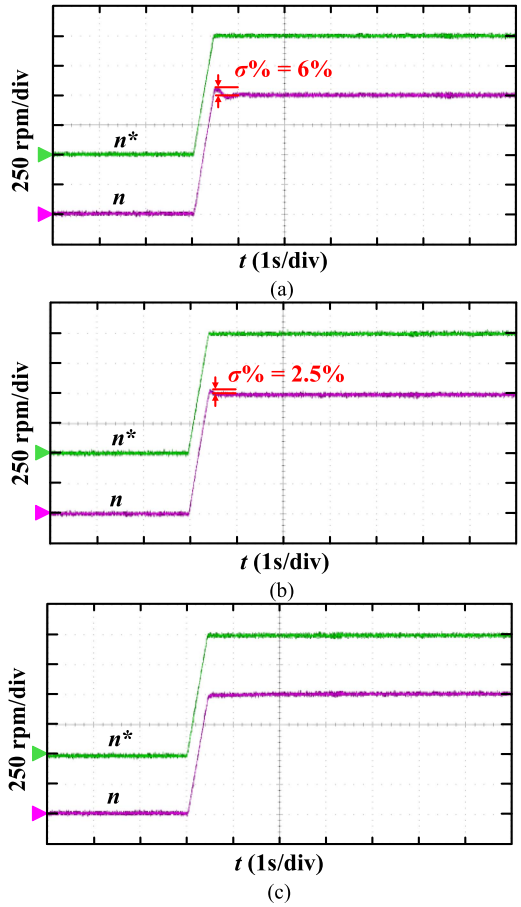

Fig. 11. Waveforms of the given speed n^* and actual speed n of IPMSM when accelerating from stop to rated speed under no-load conditions. (a) T-LADRC. (b) QPR+DDC-LADRC. (c) I-LADRC.

To verify that the I-LADRC has good dynamic performance under heavy-load conditions, the n, T_e, and i_u (U-phase current) of the motor under rated-speed operating conditions with added or subtracted heavy-load is shown in Fig. 14.

From Fig. 14, for T-LADRC, the drop of n is 15% and the dynamic response time is 0.5 s. The overshoot of n is 14.5%, the dynamic response time is 0.6 s, and there are significant speed and torque fluctuations during loading and unloading, with relatively large torque ripple. For QPR+DDC-LADRC, the drop of n is 12.5% and the dynamic response time is 0.35 s. The overshoot of n is 13%, the dynamic response time is 0.3 s, and there are slight fluctuations in the speed during loading and unloading. For I-LADRC, the drop of n is 11% and the dynamic response time is 0.2 s. The overshoot of n is 12%, the dynamic response time is 0.2 s, and there is no fluctuation in the speed during loading and unloading. This indicates that I-LADRC can suppress speed fluctuations caused by high-order interferences compared to T-LADRC and QPR+DDC-LADRC.

To verify that I-LADRC can simultaneously achieve good dynamic characteristics under heavy load conditions, suppress speed, and torque fluctuations caused by periodic interferences compared to QPR+DDC-LADRC and T-LADRC. The waveforms of n, T_e, and i_u when injecting periodic interference

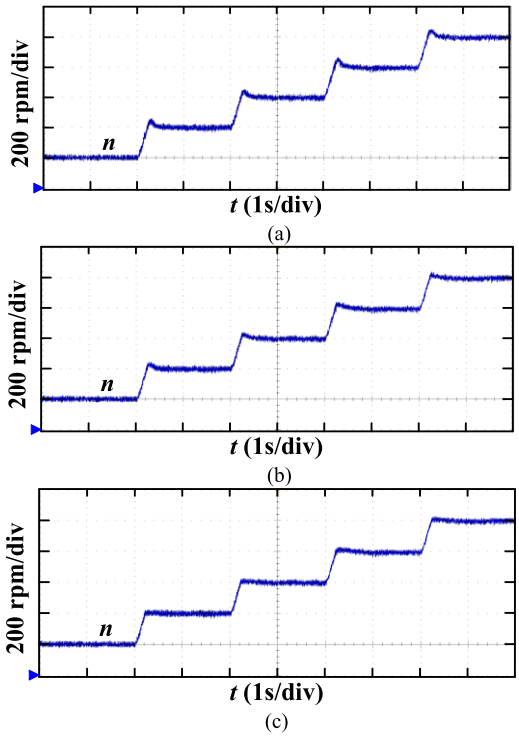

Fig. 12. Multispeed waveform under no-load conditions. (a) T-LADRC. (b) QPR+DDC-LADRC. (c) I-LADRC.

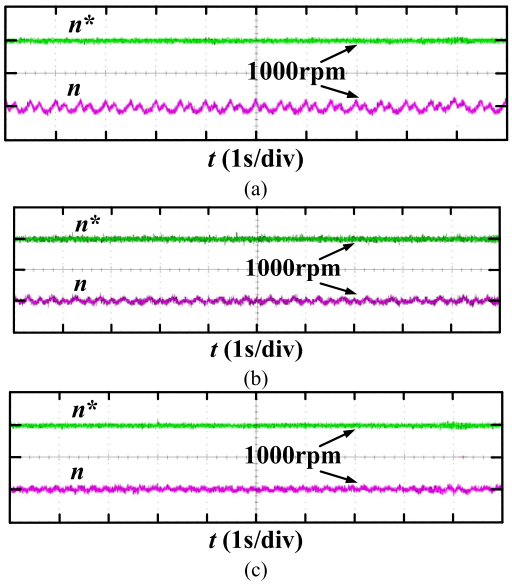

Fig. 13. Under no-load conditions, the $n*$ and n of IPMSM during steady-state operation. (a) T-LADRC. (b) QPR+DDC-LADRC. (c) I-LADRC.

signals into the system and suddenly adding or subtracting heavy loads underrated speed operating conditions are shown in Fig. 15.

From Fig. 15, under the combined influence of heavy load and periodic interference, when controlled by T-LADRC, the speed drop and overshoot of the motor during loading and unloading

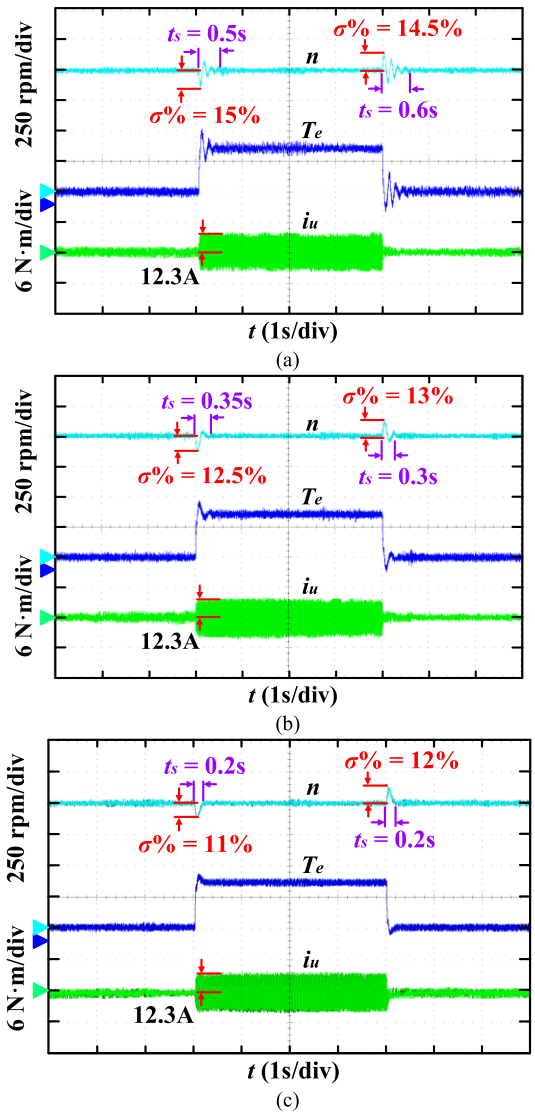

Fig. 14. n, T_e, and i_u of IPMSM during loading and unloading. (a) T-LADRC. (b) QPR+DDC-LADRC. (c) I-LADRC.

are 16.5% and 15.7%, respectively, accompanied by significant speed fluctuations and torque pulsations. When controlled by QPR+DDC-LADRC, the speed drop and overshoot of the motor during loading and unloading are both 12%, and there are still significant speed fluctuations and torque pulsations. When controlled by T-LADRC, the speed drop and overshoot of the motor during loading and unloading are 11.5% and 11%, respectively. At this time, the speed fluctuation and torque ripple are smaller compared to T-LADRC and QPR+DDC-LADRC control. This indicates that I-LADRC, compared to QPR+DDC-LADRC and T-LADRC, can simultaneously balance good dynamic characteristics under heavy load conditions and suppress speed fluctuations and torque pulsations caused by periodic interferences.

To further verify the good anti-interference characteristics of I-LADRC at different speeds, the waveforms of n and i_u of the motor under sudden load and sudden load reduction at 1000, 500, and 100 rpm are shown in Figs. 16, 17, and 18, respectively.

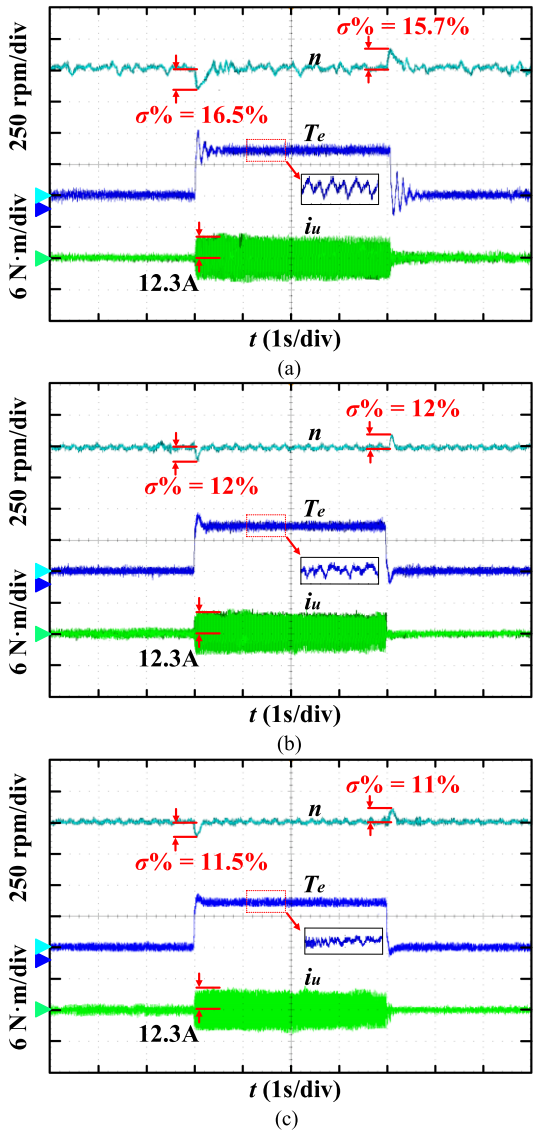

Fig. 15. When the system is simultaneously affected by periodic interferences and heavy loads, the waveforms of n, T_e, and i_u. (a) T-LADRC. (b) QPR+DDC-LADRC. (c) I-LADRC.

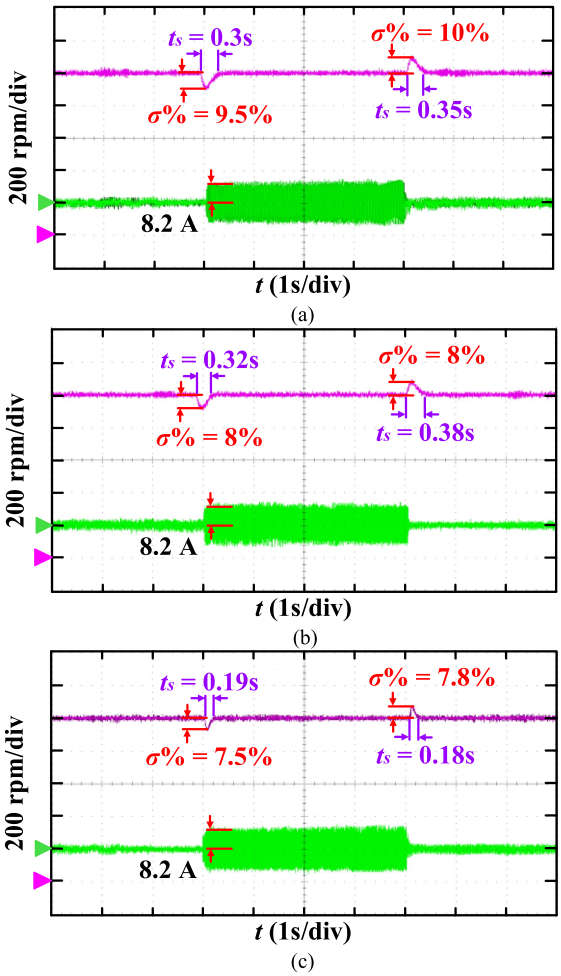

Fig. 16. Under 1000 rpm operating conditions, the n and i_u of IPMSM during loading and unloading operations. (a) T-LADRC. (b) QPR+DDC-LADRC. (c) I-LADRC.

From Fig. 16, under 1000 rpm operating conditions, for T-LADRC, the drop of n is 9.5%, and the dynamic response time is 0.3 s. The overshoot of n is 10%, and the dynamic response time is 0.35 s. For QPR+DDC-LADRC, the drop of n is 8% and the dynamic response time is 0.32 s. The overshoot of n is 8%, and the dynamic response time is 0.38 s. For I-LADRC, the drop of n is 7.5% and the dynamic response time is 0.19 s. The overshoot of n is 7.8%, and the dynamic response time is 0.18 s.

From Fig. 17, under 500 rpm operating conditions, for T-LADRC, the drop of n is 18.5% and the dynamic response time is 0.42 s. The overshoot of n is 19%, and the dynamic response time is 0.4 s. For QPR+DDC-LADRC, the drop of n is 12.5% and the dynamic response time is 0.3 s. The overshoot of n is 13%, and the dynamic response time is 0.3 s. For I-LADRC, the drop of n is 11%, and the dynamic response time is 0.22 s. The overshoot of n is 11.5%, and the dynamic response time is 0.28 s.

From Fig. 18, for T-LADRC, the drop of n is 20%, and the dynamic response time is 1.6 s. The overshoot of n is 22%, and the dynamic response time is 1.4 s. For QPR+DDC-LADRC, the drop of n is 18% and the dynamic response time is 0.3 s. The overshoot of n is 19%, and the dynamic response time is 0.38 s. For I-LADRC, the drop of n is 16% and the dynamic response time is 0.3 s. The overshoot of n is 17%, and the dynamic response time is 0.3 s.

From the abovementioned experimental results, it can be concluded that even under different operating conditions at different speeds, I-LADRC has better resistance to load interference compared to T-LADRC and QPR+DDC-LADRC.

C. Verification of Robustness

To verify that the I-LADRC can restrain the dynamic performance degradation subjected to inertia mismatch, the waveforms of n and i_u when the moment of inertia J is decreased to 0.5 J are shown in Fig. 19. The waveforms of n and i_u when the moment of inertia J is increased to 2 J are shown in Fig. 20.

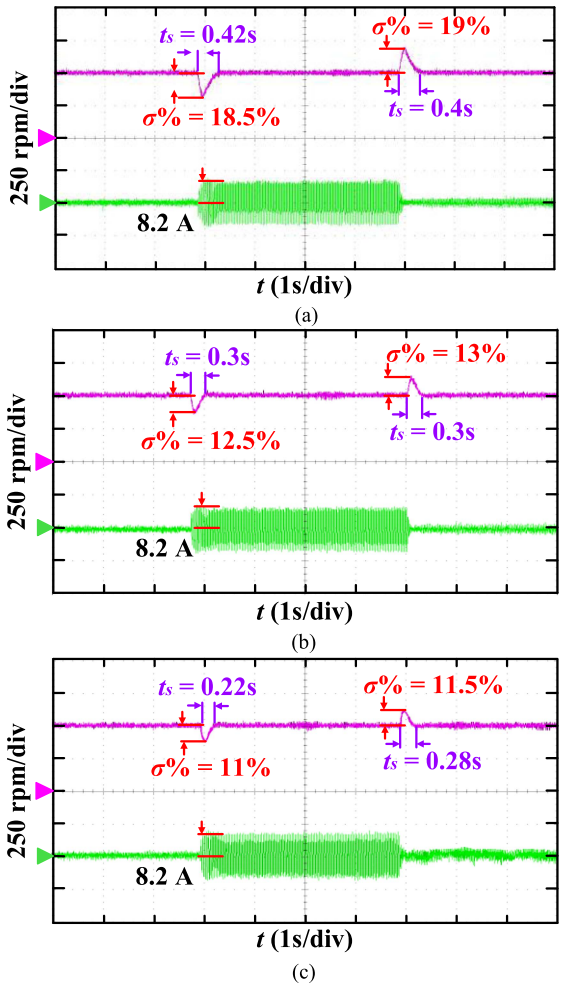

Fig. 17. Under 500 rpm operating conditions, the n and i_u of IPMSM during loading and unloading operations. (a) T-LADRC. (b) QPR+DDC-LADRC. (c) I-LADRC.

From Fig. 19, under the condition of J being decreased to 0.5 J, for T-LADRC, the drop of n is 12%, and the dynamic response time is 0.8 s. The overshoot of n is 12%, and the dynamic response time is 0.8 s. For QPR+DDC-LADRC, the drop of n is 11.5%, and the dynamic response time is 0.6 s. The overshoot of n is 11%, and the dynamic response time is 0.6 s. For I-LADRC, the drop of n is 8.5%, and the dynamic response time is 0.5 s. The overshoot of n is 8%, and the dynamic response time is 0.4 s.

From Fig. 20, under the condition of J being increased to 2 J, for T-LADRC, the drop of n is 11%, and the dynamic response time is 0.3 s. The overshoot of n is 10.5%, and the dynamic response time is 0.28 s. For QPR+DDC-LADRC, the drop of n is 10%, and the dynamic response time is 0.38 s. The overshoot of n is 10.5%, and the dynamic response time is 0.3 s. For I-LADRC, the drop of n is 9%, and the dynamic response time is 0.25 s. The overshoot of n is 10%, and the dynamic response time is 0.2 s. This indicates that compared to QPR+DDC-LADRC and T-LADRC, I-LADRC can reduce the impact of inertial mismatch.

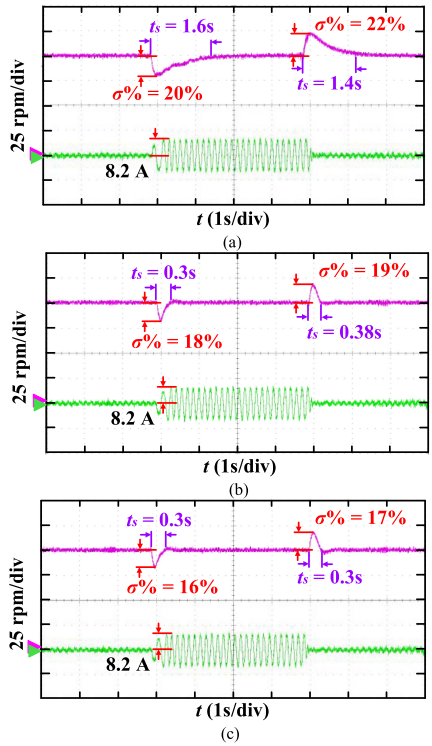

Fig. 18. Under 100 rpm operating conditions, the n and i_u of IPMSM during loading and unloading operations. (a) T-LADRC. (b) QPR+DDC-LADRC. (c) I-LADRC.

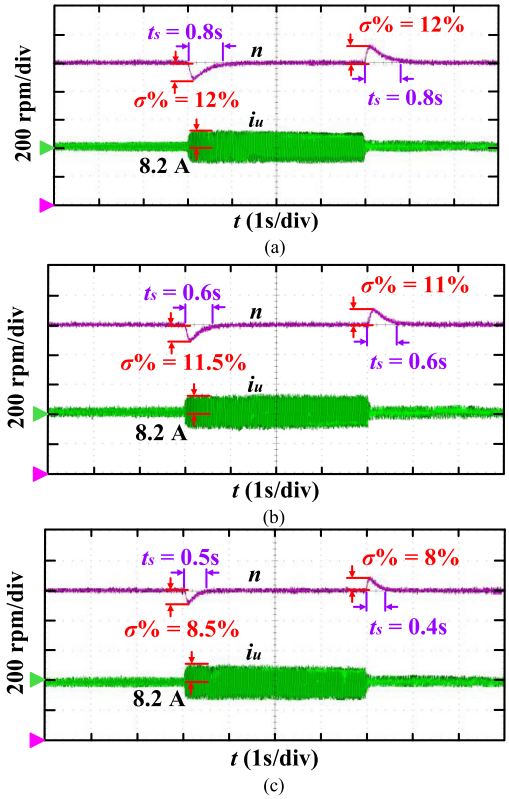

Fig. 19. Under rated-speed operating conditions, the n and i_u of IPMSM during loading and unloading operations (J decreases to 0.5 J). (a) T-LADRC. (b) QPR+DDC-LADRC. (c) I-LADRC.

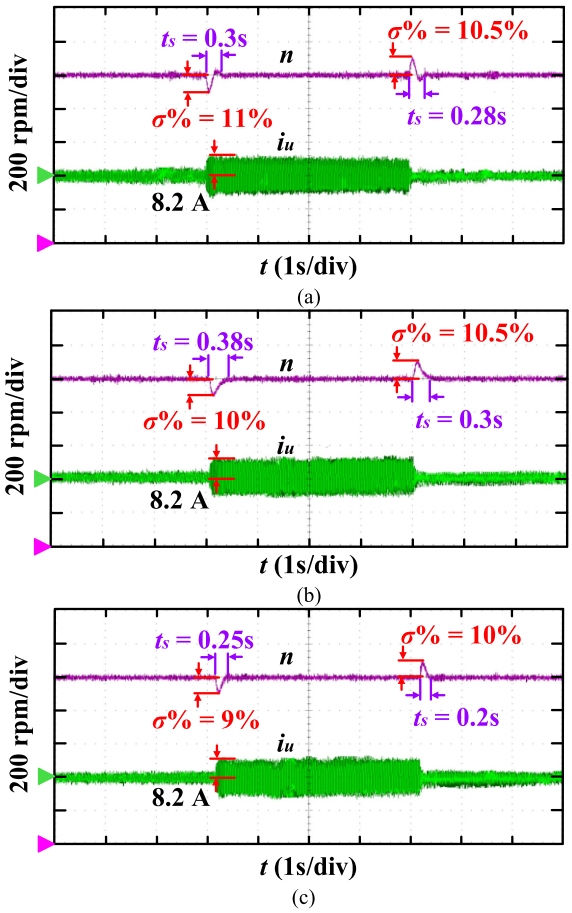

Fig. 20. Under rated-speed operating conditions, the n and i_u of IPMSM during loading and unloading operations (J increases to 2 J). (a) T-LADRC. (b) QPR+DDC-LADRC. (c) I-LADRC.

VII. Conclusion

To resolve the problem of T-LADRC inability to restrain the speed fluctuations subjected to periodic and aperiodic interferences in IPMSM control systems, an I-LADRC based on MFQRFD-LESO and G-LESO cascaded together is proposed in this article. In this controller, the interference feedforward control method of T-LESO is first changed, the ω_o and ω_c in the transfer function based on the interference term are decoupled from each other, reducing the difficulty of parameter tuning. On this basis, a multifrequency quasi-resonant filter is embedded in the decoupled LESO, so that periodic interferences can be observed in real time. For G-LESO, a fourth-order LESO is adopted to enable more accurate observation of aperiodic high-order interferences. The speed loop controller of the IPMSM control system based on I-LADRC is designed in this article, its stability and interference compensation capability are analyzed through the frequency domain analysis method. Finally, it is experimentally verified that the tracking performance, interference rejection characteristics, and robustness of this method are superior to T-LADRC.

A series of meaningful studies have been conducted in this article on the suppression of periodic and aperiodic interferences (especially high-order interferences) in the speed loop of the IPMSM drive system based on I-LADRC, aiming to reduce the speed fluctuation and torque ripple of the motor. However, there are still some problems that need further exploration and research in the future.

1) Due to hardware limitations, the system's state will be restricted. At this point, the controller proposed in this article will experience saturation and cannot continue to effectively control the system. Therefore, in the future, while improving control algorithms, it is necessary to conduct in-depth research and improvement on hardware structures.
2) Although the parameter tuning principle for the speed loop controller of the IPMSM drive system based on I-LADRC is presented in this article, compared to T-LADRC, the introduction of multifrequency quasi-resonant filters increases the difficulty of parameter tuning. Therefore, I-LADRC parameter tuning based on artificial intelligence algorithms will be a major research hotspot in the future.
3) Although the method proposed in this article can solve the inertia mismatch problem of IPMSM, the moment of inertia at this time is still a time-invariant parameter. However, when the parameters of the motor change over time in extreme environments, the problem of decreased robustness caused by time-varying parameters still cannot be effectively solved by this method. Therefore, how to improve the robustness of IPMSM driving systems under time-varying parameters through LADRC will be a key focus of future research.

References

[1] X. Li, H. Gao, W. Chen, T. Shi, and C. Xia, "Series IGBT chopping strategy based on SVPWM for PMSM drives with small DC-link capacitance," *IEEE Trans. Power Electron.*, vol. 40, no. 1, pp. 129–134, Jan. 2025.
[2] D. Zhou, K. Luo, Z. Shen, and J. Zou, "Vector-space-decomposition-based power flow control of single-stage-multiport-inverter-fed PMSM drive for hybrid electric vehicles," *IEEE Trans. Power Electron.*, vol. 71, no. 8, pp. 8514–8524, Aug. 2024.
[3] Z. Zhou, S. Zhang, Z. Xu, Y. Peng, and X. Jin, "High-quality positioning strategy for biaxial contour machining system with nonlinear model predictive control," *IEEE J. Emerg. Sel. Topics Power Electron.*, vol. 11, no. 4, pp. 4355–4367, Aug. 2023.
[4] D.-K. Hong, W. Hwang, J.-Y. Lee, and B.-C. Woo, "Design, analysis, and experimental validation of a permanent magnet synchronous motor for articulated robot applications," *IEEE Trans. Magn.*, vol. 54, no. 3, Mar. 2018, Art. no. 8201304.
[5] H. Gao, Z. Zhang, Y. Liu, W. Huang, and H. Xue, "Development and analysis of dual three-phase PMSM with phase-shifted hybrid winding for aircraft electric propulsion application," *IEEE Trans. Transp. Electrific.*, vol. 10, no. 3, pp. 6497–6508, Sep. 2024.
[6] K. Huang, W. Peng, C. Lai, and G. Feng, "Efficient maximum torque per ampere (MTPA) control of interior PMSM using sparse Bayesian based offline data-driven model with online magnet temperature compensation," *IEEE Trans. Power Electron.*, vol. 38, no. 4, pp. 5192–5203, Apr. 2023.
[7] T. Liu, M. Fadel, J. Li, and X. Ma, "A MTPA control strategy for mono-inverter multi-PMSM system," *IEEE Trans. Power Electron.*, vol. 36, no. 6, pp. 7165–7177, Jun. 2021.
[8] Y. Yan, J. Yang, Z. Sun, C. Zhang, S. Li, and H. Yu, "Robust speed regulation for PMSM servo system with multiple sources of disturbances via an augmented disturbance observer," *IEEE/ASME Trans. Mechatronics*, vol. 23, no. 2, pp. 769–780, Apr. 2018.
[9] M. Hu, W. Hua, Z. Wang, S. Li, P. Wang, and Y. Wang, "Selective periodic disturbance elimination using extended harmonic state observer for smooth speed control in PMSM drives," *IEEE Trans. Power Electron.*, vol. 37, no. 11, pp. 13288–13298, Nov. 2022.

[10] M. Tian, B. Wang, Y. Yu, Q. Dong, and D. Xu, "Robust adaptive resonant controller for PMSM speed regulation considering uncertain periodic and aperiodic disturbances," *IEEE Trans. Ind. Electron.*, vol. 70, no. 4, pp. 3362–3372, Apr. 2023.
[11] Y. Wang, P. Li, J.-X. Shen, C. Jiang, X. Huang, and T. Long, "Adaptive periodic disturbance observer based on fuzzy logic compensation for speed fluctuation suppression of PMSM under periodic loads," *IEEE Trans. Ind. Appl.*, vol. 60, no. 4, pp. 5751–5762, Jul./Aug. 2024.
[12] J. Qu, P. Zhang, and J. Jatskevich, "Harmonic current optimization for torque ripple reduction in permanent magnet synchronous machine drives based on torque ripple surrogate model," *IEEE Trans. Power Electron.*, vol. 39, no. 5, pp. 5108–5120, May 2024.
[13] B. Dai and Z. Wang, "Disturbance observer-based sliding mode control using barrier function for output speed fluctuation constraints of PMSM," *IEEE Trans. Energy Convers.*, vol. 39, no. 2, pp. 1192–1201, Jun. 2024.
[14] X. Zhang, B. Wang, Y. Yu, J. Zhang, and D. Xu, "Torque adaptive hexagon voltage extension method for PMSM flux-weakening control based on dual PI cascade structure," *IEEE Trans. Power Electron.*, vol. 38, no. 1, pp. 332–345, Jan. 2023.
[15] X. Li and R. Kennel, "General formulation of Kalman-filter-based online parameter identification methods for VSI-fed PMSM," *IEEE Trans. Ind. Electron.*, vol. 68, no. 4, pp. 2856–2864, Apr. 2021.
[16] J. Han, "From PID to active disturbance rejection control," *IEEE Trans. Ind. Electron.*, vol. 56, no. 3, pp. 900–906, Mar. 2009.
[17] Z. Gao, "Scaling and bandwidth-parameterization based controller tuning," in *Proc. Amer. Control Conf.*, 2003, pp. 4989–4996.
[18] F. Yang et al., "Complex coefficient active disturbance rejection controller for current harmonics suppression of IPMSM drives," *IEEE Trans. Power Electron.*, vol. 37, no. 9, pp. 10443–10454, Sep. 2022.
[19] Y. Cui, Z. Yin, F. Gao, Y. Zhang, Y. Liu, and J. Liu, "Speed control of IPMSM based on series connection leading correction linear active disturbance rejection controller," *IEEE Trans. Power Electron.*, vol. 39, no. 3, pp. 3096–3108, Mar. 2024.
[20] C. Wang, J. Yan, P. Heng, L. Shan, and X. Zhou, "Enhanced LADRC for permanent magnet synchronous motor with compensation function observer," *IEEE J. Emerg. Sel. Topics Power Electron.*, vol. 11, no. 3, pp. 3424–3434, Jun. 2023.
[21] Q. Xu, S. Fang, P. Wan, Y. Wang, and D. Huang, "Low-speed LADRC for permanent magnet synchronous motor with high-pass speed compensator," *IEEE J. Emerg. Sel. Topics Power Electron.*, vol. 11, no. 6, pp. 6016–6027, Dec. 2023.
[22] Z. Niu, Y. Zuo, H. Wang, L. Zhang, X. Zhu, and C. H. T. Lee, "Improved low-frequency disturbance rejection property for position control of PMSM using generalized extended state observer," *IEEE J. Emerg. Sel. Topics Power Electron.*, vol. 11, no. 5, pp. 4739–4748, Oct. 2023.
[23] X. Liu, Y. Deng, J. Wang, H. Li, and H. Cao, "Fixed-time generalized active disturbance rejection with quasi-resonant control for PMSM speed disturbances suppression," *IEEE Trans. Power Electron.*, vol. 39, no. 6, pp. 6903–6918, Jun. 2024.
[24] Q. Hou, Y. Zuo, J. Sun, C. H. T. Lee, Y. Wang, and S. Ding, "Modified nonlinear active disturbance rejection control for PMSM speed regulation with frequency domain analysis," *IEEE Trans. Power Electron.*, vol. 38, no. 7, pp. 8126–8134, Jul. 2023.
[25] G. Wang, R. Liu, N. Zhao, D. Ding, and D. Xu, "Enhanced linear ADRC strategy for HF pulse voltage signal injection-based sensorless IPMSM drives," *IEEE Trans. Power Electron.*, vol. 34, no. 1, pp. 514–525, Jan. 2019.
[26] X. Zhou, Y. Jing, Y. Ma, X. Wang, L. Tao, and H. Wen, "Active disturbance rejection and voltage stabilization control strategy for energy storage converter in microgrid based on observation state correction," *IEEE Access*, vol. 12, pp. 164588–164605, 2024.
[27] C. Dai, T. Guo, J. Yang, and S. Li, "A disturbance observer-based current-constrained controller for speed regulation of PMSM systems subject to unmatched disturbances," *IEEE Trans. Ind. Electron.*, vol. 68, no. 1, pp. 767–775, Jan. 2021.
[28] S. Li, Y. Xu, W. Zhang, and J. Zou, "Robust deadbeat predictive direct speed control for PMSM with dual second-order sliding-mode disturbance observers and sensitivity analysis," *IEEE Trans. Power Electron.*, vol. 38, no. 7, pp. 8310–8326, Jul. 2023.
[29] Y. Zuo, J. Chen, X. Zhu, and C. H. T. Lee, "Different active disturbance rejection controllers based on the same order GPI observer," *IEEE Trans. Ind. Electron.*, vol. 69, no. 11, pp. 10969–10983, Nov. 2022.
[30] S. Zhu, W. Wang, Y. Zhao, X. Lin, and D. Dong, "Robust speed control of electrical drives with reduced ripple using adaptive switching high-order extended state observer," *IEEE Trans. Power Electron.*, vol. 37, no. 2, pp. 2009–2020, Feb. 2022.
[31] Y. Zuo, J. Mei, C. Jiang, X. Yuan, S. Xie, and C. H. T. Lee, "Linear active disturbance rejection controllers for PMSM speed regulation system considering the speed filter," *IEEE Trans. Power Electron.*, vol. 36, no. 12, pp. 14579–14592, Dec. 2021.
[32] J. Xu, Z. Wei, and S. Wang, "Active disturbance rejection repetitive control for current harmonic suppression of PMSM," *IEEE Trans. Power Electron.*, vol. 38, no. 11, pp. 14423–14437, Nov. 2023.
[33] Y. Wang, L. Tao, P. Wang, X. Ma, P. Cheng, and D. Zhao, "Improved linear ADRC for hybrid energy storage microgrid output-side converter," *IEEE Trans. Ind. Electron.*, vol. 69, no. 9, pp. 9111–9120, Sep. 2022.
[34] Y. Cui, Z. Yin, X. Cao, Y. Zhang, and Y. Liu, "Enhanced linear active disturbance rejection speed control of IPMSM based on interference differential compensation and cascaded linear extended state observer," *IEEE Trans. Power Electron.*, vol. 39, no. 10, pp. 13582–13596, Oct. 2024.
[35] M. Tian, B. Wang, Y. Yu, Q. Dong, and D. Xu, "Adaptive active disturbance rejection control for uncertain current ripples suppression of PMSM drives," *IEEE Trans. Ind. Electron.*, vol. 71, no. 3, pp. 2320–2331, Mar. 2024.
[36] H. Cao et al., "Improved ADRC with a cascade extended state observer based on quasi-generalized integrator for PMSM current disturbances attenuation," *IEEE Trans. Transp. Electrific.*, vol. 10, no. 1, pp. 2145–2157, Mar. 2024.
[37] B. Wang, M. Tian, Y. Yu, Q. Dong, and D. Xu, "Enhanced ADRC with quasi-resonant control for PMSM speed regulation considering aperiodic and periodic disturbances," *IEEE Trans. Transp. Electrific.*, vol. 8, no. 3, pp. 3568–3577, Sep. 2022.
[38] Y. Cui, Z. Yin, P. Luo, D. Yuan, and J. Liu, "Linear active disturbance rejection control of IPMSM based on quasi-proportional resonance and disturbance differential compensation linear extended state observer," *IEEE Trans. Ind. Electron.*, vol. 71, no. 10, pp. 11910–11924, Oct. 2024.

Yangyang Cui was born in Shandong, China, in 1996. He received the B.S. degree in electrical engineering and automation from the Shandong University of Aeronautics, Binzhou, China, in 2018, and the M.S. degree in electrical engineering from the Tianjin University of Technology, Tianjin, China, in 2021. He is currently working toward the Ph.D. degree in electrical engineering with the Xi'an University of Technology, Xi'an, China.

His current research focuses on advanced control theory and technology for high-performance ac motors.

Zhonggang Yin (Member, IEEE) was born in Shandong, China, in 1982. He received the B.S., M.S., and Ph.D. degrees in electrical engineering from the Xi'an University of Technology, Xi'an, China, in 2003, 2006, and 2009, respectively.

In 2009, he joined the Electrical Engineering Department, Xi'an University of Technology, where he is currently a Professor. His research interests include high-performance control of ac motor and digital control of power converters.

Yanping Zhang (Member, IEEE) was born in Shaanxi, China, in 1989. He received the B.S. degree in electrical engineering from Xi'an Polytechnic University, Xi'an, China, in 2013, and the M.S. and Ph.D. degrees in electrical engineering from Xi'an University of Technology, Xi'an, China, in 2017 and 2021, respectively.

In 2021, he joined the Electrical Engineering Department, Xi'an University of Technology, where he is currently a Lecturer. His research interest includes high-performance sensorless control of synchronous motors.

Hui Yang received the B.S., M.S., and Ph.D. degrees in electrical engineering from the Xi'an University of Technology, Xi an, China, in 2001, 2007, and 2018, respectively.

Since 2004, she has been with Xi'an University of Technology, where she is currently an Assistant Professor with the School of Electrical Engineering. From 2019 to 2020, she was a Visiting Scholar with FEEC, Virginia Tech University, USA. Her research interests include distributed power systems, digital control of power converters, and energy storage systems.